Coordination Chemistry Reviews 254 (2010) 1054–1071

Contents lists available at ScienceDirect

Coordination Chemistry Reviews

journal homepage: www.elsevier.com/locate/ccr

Review

Colloidal chemical approaches to inorganic micro- and nanostructures with controlled morphologies and patterns

Limin Qi*

College of Chemistry, Peking University, Beijing 100871, PR China

Contents

ARTICLE INFO

Article history:
Received 1 December 2009
Accepted 4 February 2010
Available online 12 February 2010

Keywords:
Micro-/nanostructures
Morphology
Pattern
Catanionic micelles
Reactive templates
Colloidal crystals

ABSTRACT

The controlled synthesis of inorganic micro- and nanostructures with tailored morphologies and patterns has attracted intensive interest because the properties and performances of micro- and nanostructured materials are largely dependent on the shape and structure of the primary building blocks and the way in which the building blocks are assembled or integrated. This review summarizes the recent advances on the solution-phase synthesis of inorganic micro- and nanostructures with controlled morphologies and patterns via three typical colloidal chemical routes, i.e., synthesis based on catanionic micelles, reactive templates, and colloidal crystal templates, with focus on the approaches developed in our lab. Firstly, catanionic micelles formed by mixed cationic/anionic surfactants are used as effective reaction media for the shape-controlled synthesis of inorganic nanocrystals and the solution growth of hierarchical superstructures assembled by one-dimensional (1D) nanostructures. Secondly, reactive template-directed chemical transformation strategy provides a simple and versatile route to fabricate both hollow structures and 1D nanostructures. Thirdly, colloidal crystals are employed as very effective templates for the facile solution-phase synthesis of novel inorganic structures with controlled patterns, such as three-dimensionally (3D) ordered macroporous materials and two-dimensionally (2D) patterned nanoarrays and nanonets. Finally, a brief outlook on the future development in this area is presented.

1. Introduction

In recent years, the controlled synthesis of inorganic micro- and nanostructures with tailored morphologies and patterns has attracted intensive interest because the properties and performances of micro- and nanostructured materials are largely dependent on the shape and structure of the primary building blocks and the way how the building blocks are assembled or integrated. The size and shape of nanocrystals are key factors for the determination of their chemical and physical properties [1]. In this regard, significant effort has been devoted to the shape-controlled synthesis of colloidal nanocrystals of metals, semiconductors, and metal oxides since such shape-controlled nanocrystals may find wide potential applications in catalysis and optical, electronic, magnetic, and sensory devices, and as building blocks for bottom-up assembly [2–5]. In particular, shape-controlled

* Tel.: +86 10 62751722.
E-mail address: liminqi@pku.edu.cn.

0010-8545/$ – see front matter © 2010 Elsevier B.V. All rights reserved.
doi:10.1016/j.ccr.2010.02.005

metal and semiconductor nanocrystals have demonstrated unique properties and superior performance in catalysis. For example, tetrahexahedral Pt nanocrystals enclosed by 24 high-index facets exhibited much enhanced (up to 400%) catalytic activity for equivalent Pt surface areas for electro-oxidation of small organic fuels [6], while tetrahedral Pt nanoparticles, which expose (1 1 1) facets exclusively, selectively promoted the *trans*-to-*cis* isomerization of olefins, demonstrating remarkable catalysis selectivity controlled by particle shape [7]. Recently, it was reported that Pd–Pt bimetallic nanodendrites consisting of a dense array of Pt branches on faceted Pd nanocrystals exhibited high catalytic activity towards the oxygen reduction [8]. Moreover, it has been demonstrated that semiconductor anatase crystals with a high percentage of highly reactive {0 0 1} facets can be fabricated by using a suitable morphology controlling agent [9]; thereafter, rectangular TiO_2 nanosheets with (0 0 1) facets as the top and bottom surfaces were successfully synthesized and they showed excellent photocatalytic efficiency [10]. Much recent effort has been focused on the assembly and integration of nanoscale building blocks into ordered superstructures or complex functional architectures, which is essential for the success of bottom-up approaches towards future nanodevices and would offer opportunities to explore their novel collective properties and improve our understanding of self-assembly processes occurring on molecular to macroscopic length scales [11–16].

Among nanoscale building blocks with various shapes, one-dimensional (1D) nanostructures such as wires, rods, belts and tubes provide an ideal system to investigate the dimensionality and size dependence of the electrical and optical properties of nanomaterials, and they are expected to play an important role as both interconnects and functional units in fabricating electronic, optoelectronic, electrochemical, and electromechanical devices with nanoscale dimensions [17–20]. On the other hand, inorganic hollow structures of nanometer to micrometer dimensions represent an important class of materials that have advantageous properties including high surface area, low density, and large fraction of void space as well as potential applications in controlled drug delivery, catalysis, sensors, lightweight fillers, low-dielectric-constant thin films, confined-space chemical reactors, biomedical diagnosis and therapy, and so on [21–24]. Hence the controlled synthesis of 1D nanostructures and hollow micro-/nanostructures has been the focus of extensive research.

In addition to the preparation of individual building blocks, the fabrication of large-area or macroscopic functional materials patterned on the micro- and nanometer scale is receiving increasing interest. In this regard, the assembly of three-dimensional (3D) colloidal crystals with adjustable structures and the fabrication of their inversely replicated functional materials such as three-dimensionally ordered macroporous (3DOM) materials have attracted much attention mainly due to their promising applications as photonic crystals, catalysts, sensors, porous electrodes, substrates for surface-enhanced Raman scattering (SERS), and in separation technology and other emerging nanotechnologies [25–28]. Moreover, nanoporous and nanostructured films have become increasingly important to the microelectronics and photonics industries and they exhibit tremendous potential for separations, catalytic, biomedical and heat transfer applications [29]. Furthermore, the rational engineering of surface architectures has enabled many exciting observations, especially when micro- or nanofeatures are arranged on surfaces resulting in two-dimensional (2D) ordered patterns [30–32].

Generally, colloidal chemical approaches are solution-phase synthetic methods based on wet chemical reactions and they have been widely used for the shape-controlled synthesis of inorganic nanocrystals [33,34]. Compared to the gas-phase growth process, colloidal chemical routes have advantages such as relatively low temperatures, cheap instruments, convenience in handling, and easiness in composition control, which make it very promising for the large-scale and environmentally benign synthesis of morphology-controlled inorganic micro- and nanostructures. This review summarized our recent endeavors on the controlled synthesis of inorganic micro- and nanostructures with tailored morphologies and patterns via three typical colloidal chemical routes, i.e., synthesis based on catanionic micelles, reactive templates, and colloidal crystal templates. Firstly, catanionic micelles formed by mixed cationic/anionic surfactants turn out to be effective reaction media for the shape-controlled synthesis of inorganic nanocrystals and the solution growth of hierarchical superstructures assembled by 1D nanostructures. Secondly, reactive template-directed chemical transformation strategy provides a simple and versatile route to fabricate both hollow structures and 1D nanostructures. Thirdly, colloidal crystals have been demonstrated to be versatile templates for the facile solution-phase synthesis of novel inorganic structures with controlled micro- and nanopatterns, such as 3DOM single crystals, 2D patterned nanopillar arrays, and free-standing highly-ordered nanonets. Finally, a brief outlook on the future development in this area is presented.

2. Synthesis based on catanionic micelles

Catanionic micelles are micellar aggregates self-assembled by mixed cationic/anionic surfactants in continuous oil phase (i.e., reverse micelles) or water phase (i.e., normal micelles). Such catanionic micelles have a unique interfacial film of mixed surfactants and contain binary surfactants that could provide synergistic effects on the crystal nucleation and growth. Therefore, both catanionic reverse micelles and catanionic normal micelles have turned out to be very effective in the morphological control of inorganic nanostructures.

2.1. Reverse micelles

Reverse micelles and microemulsions are powerful as nanostructured media or nanoreactors for the controlled synthesis of inorganic nanostructures [35,36]. In most cases, spherical nanoparticles are obtained in reverse micelles where the surfactant-stabilized water nanodroplets play the role of nanoreactors. However, 1D nanostructures with high aspect ratios can also be synthesized by using reverse micelle solutions in specific cases. For example, we first reported the synthesis of single-crystalline, *c*-axis-oriented $BaCO_3$ nanowires with aspect ratios as large as 10 000 in nonionic reverse micelles of $C_{12}E_4$ (tetraethylene glycol monododecyl ether) in cyclohexane [37]. The obtained nanowires were 10–30 nm in diameter and up to 100 μm in length, which formed a rather regular 2D nanowire array in a large area upon deposition on a Formvar-covered copper grid. According to time-dependent TEM (transmission electron microscopy) observations of the crystal growth process, a directional (or oriented) aggregation mechanism was proposed for the nanowire formation in reverse micelles. Later on, nanorods and nanobelts of the Prussian blue (PB) analogue $SmFe(CN)_6{\cdot}4H_2O$ were successfully synthesized in reverse micelles formed by the nonionic surfactant polyoxyethylene (5) nonylphenyl ether (NP-5) and the cationic surfactant cetyltrimethyl-ammonium bromide (CTAB), respectively [38]. The related magnetic studies showed that the shape of the low-dimensional magnetic nanomaterial is a dominating factor for its coercivity due to the effect of shape anisotropy.

While reverse micelles formed by single surfactants have been widely employed for the synthesis of inorganic nanostructures, catanionic reverse micelles formed by mixed cationic/anionic surfactants were not used for the inorganic synthesis until 2002 [39]. The catanionic reverse micelles show a unique interfacial film formed by mixed surfactants and the state of interfacial film

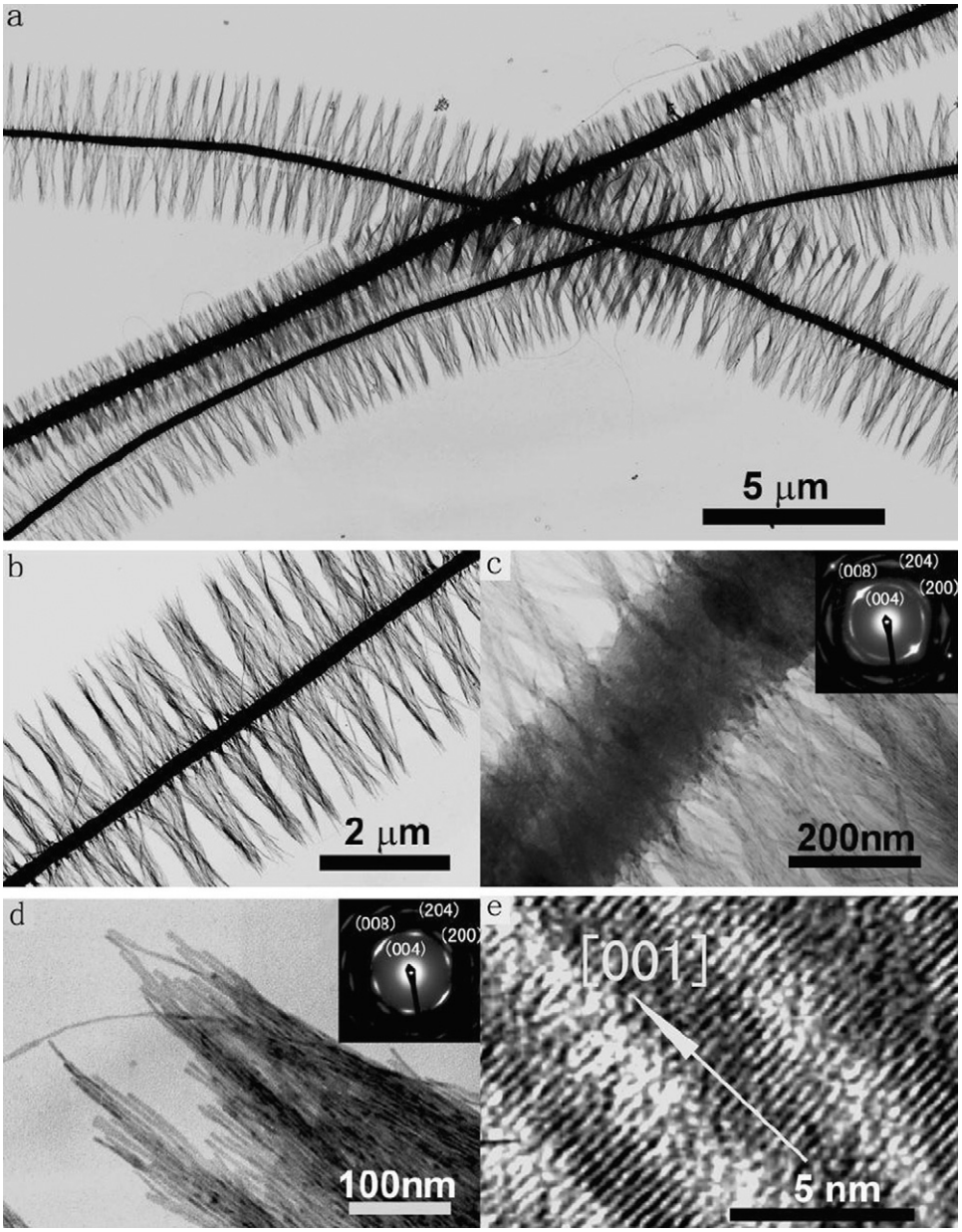

Fig. 1. TEM (a–d) and HRTEM (e) images of penniform $BaWO_4$ nanostructures obtained in the presence of PEG-*b*-PMAA. Insets show the corresponding ED patterns. Reprinted with permission from Ref. [40]. Copyright 2003 American Chemical Society.

is largely determined by the mixing ratio between anionic and cationic surfactants (r). When r equals to 1, the mixed surfactant film stays in a tight state. If anionic and catanionic surfactants are mixed in non-equimolar ratios, i.e., $r > 1$ or $r < 1$, the mixed surfactant monolayer would become looser because of the electrostatic repelling force between the ionic heads of the excess surfactant molecules. A catanionic reverse micelle system consisting of water, decane, and a mixture of two surfactants: undecylic acid and decyl amine, where the cationic surfactant was produced by the protonation of the amine by undecylic acid, was first selected for the synthesis of $BaWO_4$ nanowires. Notably, high aspect-ratio, single-crystalline $BaWO_4$ nanowires with diameters as small as 3.5 nm and lengths up to more than 50 μm were successfully synthesized in catanionic reverse micelles formed by an equimolar mixture of undecylic acid and decyl amine, indicating the great potential of such catanionic reverse micelles in the fabrication of ultrathin inorganic nanowires.

Interestingly, unique penniform $BaWO_4$ nanostructures were readily obtained when a double-hydrophilic block copolymer, poly(ethylene glycol)-*block*-poly(methacrylic acid) (PEG-*b*-PMAA), was introduced into the catanionic reverse micelle system [40]. Fig. 1 presents the typical TEM images of the obtained penniform $BaWO_4$ nanostructures at different magnifications. The low-magnification image in Fig. 1a shows that the product exhibits a feather-like appearance with numerous, nearly parallel barbs grown perpendicular on both sides of a shaft. In general, the "feathers" are up to 50 μm in length and ranging from 2.5 to 4.5 μm in width and the diameters of the shafts lies in the range of 200–400 nm. Fig. 1b shows an enlarged image of a single feather, which has a shaft ~230 nm in diameter and two feathery tufts about 2 μm in length. A high-magnification image of the central part of the feather (Fig. 1c) suggests that the slender, parallel barbs are actually $BaWO_4$ nanowires grown perpendicular on the shaft. A high-magnification image of a feathery tuft of the feather (Fig. 1d)

clearly shows the nanowires are uniform in diameter (~3.5 nm). The related electron diffraction (ED) pattern is consistent with pure $BaWO_4$ crystals of a tetragonal scheelite structure and indicates that each nanowire is a single crystal with the *c* axis along the length axis, which is very similar to that for the $BaWO_4$ nanowires obtained in the reverse micelles in the absence of the polymer. A typical high resolution TEM (HRTEM) image shown in Fig. 1e confirms that the $BaWO_4$ nanowires are single crystals grown preferentially along their *c* axes. Comparing with the ED pattern obtained from the edge of a feathery tuft (Fig. 1d), the ED pattern obtained from the shaft together with a few adjacent nanowires (Fig. 1c) exhibits similar diffraction spots as well as discontinuous rings rather than full rings, indicating that the shaft itself could consists of $BaWO_4$ polycrystals with their crystallographic [0 0 1] axis orientated nearly perpendicular to the shaft. This is the first solution growth of hierarchical architectures consisting of regularly aligned inorganic nanowires. This approach may open new routes towards bottom-up integration of one-dimensional (1D) building blocks into two-dimensional (2D) and three-dimensional (3D) ordered superstructures or complex functional architectures.

The growth mechanism of penniform $BaWO_4$ nanostructures in catanionic reverse micelles involving the polymer PEG-*b*-PMAA has been investigated in detail [41]. The $BaWO_4$ crystallization was first performed in aqueous solution in the presence of PEG-*b*-PMAA to examine the effect of the polymer as an additive on the crystallization of $BaWO_4$ crystals, which suggested that PEG-*b*-PMAA could induce the formation [0 0 1]-oriented shuttle-like $BaWO_4$ crystals in aqueous solution. Then, a careful examination of the $BaWO_4$ nanostructures obtained at different periods of aging time in catanionic reverse micelles indicated a two-stage growth mechanism for the penniform nanostructures, i.e., the formation of the [1 0 0]-oriented shaft and the subsequent growth of [0 0 1]-oriented nanowires perpendicularly on both sides of the shaft in parallel. Moreover, it was revealed that the *a*-axis-oriented shafts formed by oriented attachment and fusion of preformed *c*-axis-oriented shuttle-like $BaWO_4$ nanocrystals along the [1 0 0] axis of the scheelite lattice. Furthermore, penniform nanostructures consisting of [0 0 1]-oriented $BaWO_4$ nanobelts grown perpendicularly on both sides of a shaft were obtained at $r = 1.2$ or $r = 0.4$, i.e., in the presence of excess undecylic acid or decyl amine in the surfactant mixture.

Accordingly, a detailed two-stage growth mechanism has been proposed based on the experimental observations (Scheme 1) [41]. The formation of the penniform nanostructures is divided into two growth stages, i.e., the polymer-controlled shaft formation (Stage 1) and the mixed surfactants-controlled barb growth (Stage 2). During Stage 1, the polymer PEG-*b*-PMAA participated in the precipitation process of $BaWO_4$ in aqueous cores of catanionic reverse micelles and induced the formation of *c*-axis-oriented shuttle-like nanocrystals. Then, the side-by-side assembly and fusion of the shuttle-like nanocrystals via oriented attachment along the [1 0 0] direction resulted in the formation of [1 0 0]-oriented prickly shafts with many [0 0 1]-oriented needles grown perpendicularly on both sides of the shaft in parallel. The gradual adsorption of PEG-*b*-PMAA molecules on the growing shafts would lead to a considerable decrease of the concentration of free polymer molecules in solution, which could finally result in the transition of the crystal growth process from Stage 1 to Stage 2 due to the low polymer concentration in solution. During Stage 2, [0 0 1]-oriented nanowires or nanobelts grew gradually from the needles at approximately equal growth rates, leading to the formation of well-defined penniform $BaWO_4$ nanostructures. The morphology of the feather barbs was essentially determined by the mixing ratio *r* of the anionic to cationic surfactants, i.e., [0 0 1]-oriented nanowires were formed at $r = 1$ while [0 0 1]-oriented nanobelts with the (1 0 0) top surface either perpendicular or parallel to the [1 0 0] direction of the shaft were formed at *r* deviating from 1. This understanding of the growth mechanism of penniform $BaWO_4$ nanostructures in catanionic reverse micelles involving polymers may be potentially applied for designing new synthesis system for the controlled synthesis of other hierarchical 1D nanostructures with desired architectures.

The synthesis of hierarchical nanowire/nanobelt superstructures in catanionic reverse micelles can be extended to other material systems including $BaCrO_4$ and $BaMoO_4$. For example, a variety of $BaCrO_4$ nanostructures, such as nanowires, nanobelts, and tree-like superstructures, were obtained in catanionic reverse micelles without polymers by simply changing the mixing ratio *r* [42]. At a mixing ratio $r = 1$, i.e., in the presence of equimolar undecylic acid and decyl amine, bundles of $BaCrO_4$ nanowires were obtained. If *r* was increased to larger than 1, i.e., in the presence of excess undecylic acid, $BaCrO_4$ nanobelts as well as their unique assemblies showing tree-like superstructures can be obtained. At $r = 1.4$, the obtained product was bundles of $BaCrO_4$ nanobelts. When *r* was increased to 1.7, hierarchical, tree-like $BaCrO_4$ superstructures (~10 μm in length), which consisted of branches with numerous, nearly parallel nanoleaflets grown on

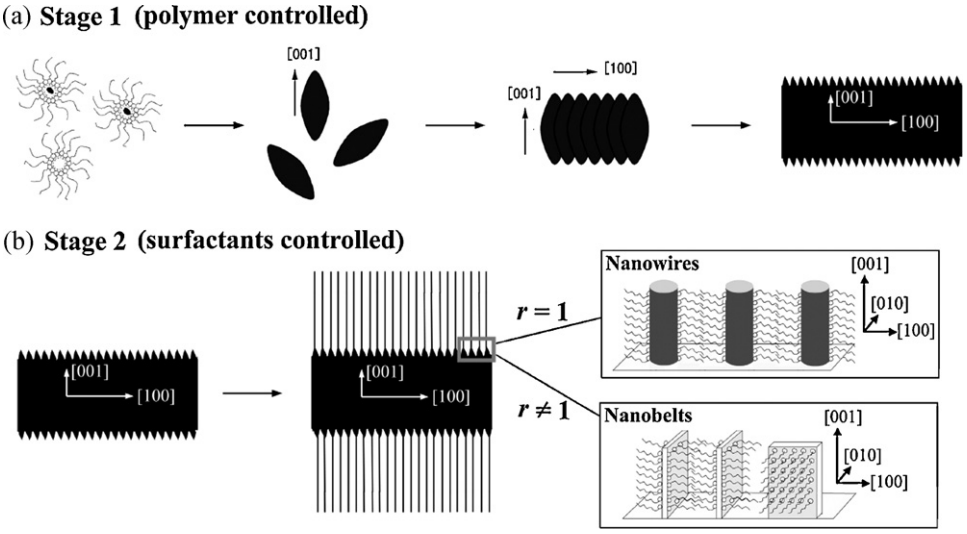

Scheme 1. Schematic illustration of the detailed formation of penniform $BaWO_4$ nanostructures. Reprinted with permission from Ref. [41]. Copyright 2006 American Chemical Society.

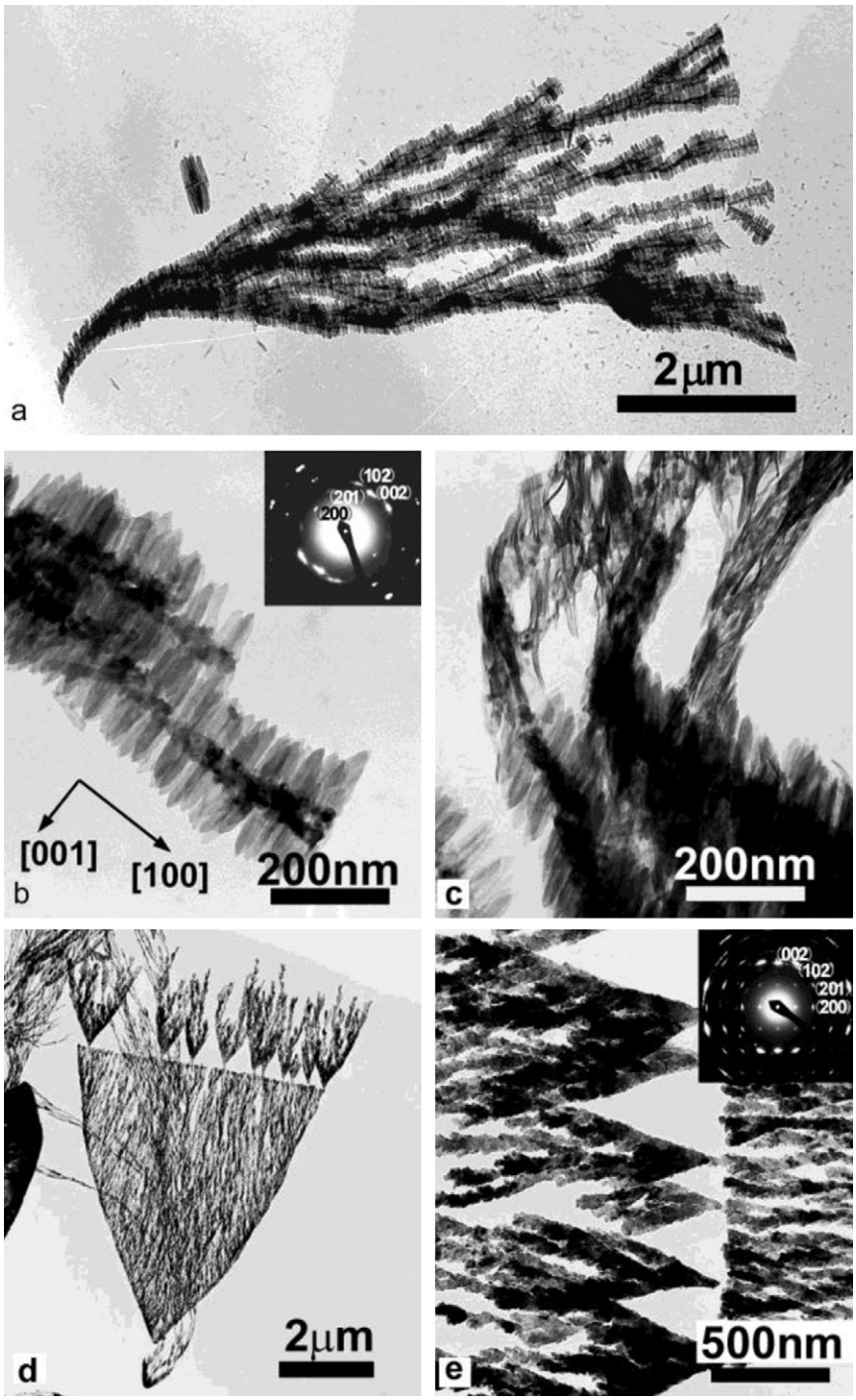

Fig. 2. TEM images of tree-like $BaCrO_4$ superstructures formed at $r = 1.7$ (a–c) and $r = 2$ (d and e). Insets show the corresponding ED patterns. Reprinted with permission from Ref. [42]. Copyright 2003 Wiley-VCH.

two opposite sides, were produced (Fig. 2a). The branches were about 40 nm in width and the nanoleaflets grown on the branches about 100 nm in length, 20 nm in width (Fig. 2b). The twisted branched shown in Fig. 2c clearly revealed that the nanoleaflets were nanobelts with a thickness about 4 nm. The ED pattern corresponding to a single branch containing leaflets indicated that the whole branch was orthorhombic $BaCrO_4$ crystals with the *a* axis along the length direction and the *c* axis along the width direction, which suggested that the nanoleaflets grew in length along the *c* axis and width along the *a* axis, consistent with the growth direction of the $BaCrO_4$ nanobelts obtained at $r = 1.4$. If *r* was further increased to 2, bare-tree-like $BaCrO_4$ superstructures showing self-similarity were obtained (Fig. 2d). An enlarged image (Fig. 2e) revealed that there were no nanoleaflets grown on the branches but there were secondary trees grown on the sharp growth front of the primary tree. The related ED pattern indicated that the bare branches were $BaCrO_4$ crystals gown along the [1 0 0] direction, similar to the growth direction of the branches containing nanoleaflets.

The effect of the mixing ratio *r* on the morphology of $BaCrO_4$ nanostructures could be tentatively explained by assuming that the interfacial film with varied *r* values would preferentially adsorb

on specific faces of $BaCrO_4$ crystals due to interfacial molecular recognition and thus induce preferential crystal growth. At $r = 1$, undecylic acid could preferentially adsorb on surfaces parallel to the *c* axis, resulting in the formation of $BaCrO_4$ nanowires along [0 0 1] direction. At $r = 1.4$, undecylic acid could preferentially adsorb on the (0 1 0) surface, resulting in the formation of $BaCrO_4$ nanobelts showing (0 1 0) top surface and grown along the [0 0 1] direction. When *r* was increased to 2, undecylic acid could preferentially adsorb on surfaces parallel to the *a* axis, resulting in the formation of tree-like $BaCrO_4$ superstructures with bare branches along the [1 0 0] direction. When *r* lies between 1.4 and 2, for instance, $r = 1.7$, undecylic acid could preferentially adsorb on surfaces parallel to the *a* axis at the beginning, resulting in the formation of bare braches; On crystal growing, the proportion of undecylic acid in the remaining mixed film could decrease due to preferential adsorption of undecylic acid on the crystals, leading to the growth of nanoleaflets showing (0 1 0) top surface as in the case of $r = 1.4$.

In addition, $BaMoO_4$ nanobelts and their hierarchical superstructures were synthesized in the catanionic reverse micelles without polymers [43]. Architectural control of the hierarchical nanobelt superstructures was readily achieved by changing the mixing ratio *r* and the reaction temperature. At a suitable surfactant mixing ratio ($r = 1.5$), two different kinds of penniform $BaMoO_4$ nanobelt superstructures, i.e., one consisting of [0 0 1]-oriented nanobelts grown obliquely on a [2 0 4]-oriented shaft and the other consisting of [0 0 1]-oriented nanobelts grown perpendicularly on a [1 0 0]-oriented shaft, were produced at 50 °C and 30 °C, respectively. This result further suggested that such catanionic reverse micelles may represent promising nanostructured media for solution synthesis of inorganic nanobelts and their hierarchical assembly into complex nanobelt superstructures.

The catanionic reverse micelle systems used for the nanostructure synthesis can be extended from the current system made of undecylic acid and decyl amine to other surfactant systems. For example, the synthesis of gold nanoparticles in catanionic reverse micelles formed by octanoic acid and octylamine was recently reported [44]. Notably, nanofilaments/nanorods of cerium phosphate and cobalt phosphate, which were highly uniform in width (4–5 nm) and variable in length (up to 1200 nm), were successfully synthesized in catanionic reverse micelles formed by hexadecyltrimethylammonium phosphate [$(CTA)_3PO_4$] and cerium or cobalt bis(2-ethylhexyl) sulfosuccinate [$Ce(AOT)_3$ or $Co(AOT)_2$] [45]. Whereas the particle width was constrained by the size of the catanionic reverse micelles, changes in the reaction conditions such as the concentration of the surfactant salts and [$Ce(AOT)_3$]/[$(CTA)_3PO_4$] molar ratio, markedly influenced the length of the inorganic nanostructures. The $CePO_4$ nanofilaments were crystalline and morphologically invariant with regard to changes in the reaction conditions, whereas the $Co_3(PO_4)_2$ nanorods were amorphous and more sensitive to modifications in the mixing molar ratio of the two surfactants. It should be pointed out that the further application of the catanionic reverse micelles as reaction media would largely rely on the understanding of the microstructure of the reverse micelles as well as their interaction with inorganic crystals at the molecular level. In this regard, a variety of experimental techniques, such as conductivity measurements, small-angle neutron scattering (SANS), dynamic light scattering (DLS), steady-state and time-resolved fluorescence emission, and time-resolved fluorescence anisotropy, have been employed to investigate the microstructures of various catanionic reverse micelles [46,47]. Meanwhile, in situ time-resolved small-angle X-ray scattering (SAXS) measurements have been performed to reveal the variation of the microstructure of catanionic reverse micelles during the whole reaction of the Au nanoparticle synthesis [44].

2.2. Normal micelles

While catanionic reverse micelles have shown great potential in the morphology-controlled synthesis of inorganic nanostructures, a large amount of organic solvents are used to constitute the continuous medium of the reverse micelles, which is not desirable from environmental consideration. On the other hand, catanionic normal micelles formed by mixed cationic/anionic surfactants in aqueous solution are environmentally benign and hence relatively green synthesis could be realized if such catanionic normal micelles are used for the morphology-controlled synthesis of inorganic nanostructures. Due to the absence of aqueous nanodroplets, normal micelles generally cannot act as nanoreactors for the space-confined synthesis of nanostructures as in the case of reverse micelles. However, the aqueous micellar solution consisting of mixed cationic/anionic surfactants could play special roles in the crystal nucleation and growth owing to the synergistic interactions of the binary surfactants with reactants ions as well as specific crystal planes, leading to an effective morphological control of the formed nanostructures.

As a π–π semiconductor with a narrow band gap (0.41 eV) and a large exciton Bohr radius (18 nm), PbS shows extensive quantum size effects for nanocrystals and has wide-ranging potential applications such as near-IR communication, optical switches, thermal and biological imaging, photovoltaics, and solar cells. While star-shaped PbS nanocrystals were successfully produced by the thermal decomposition of a molecular precursor in a hot phenyl ether solvent at 230 °C [48], uniform star-shaped PbS nanocrystals with six symmetric horns were successfully synthesized in aqueous solutions of catanionic normal micelles at a low temperature of 80 °C [49]. The synthesis of star-shaped PbS nanocrystals was achieved by the thermal decomposition of thioacetamide (TAA) in aqueous solutions of lead acetate in the presence of the cationic surfactant CTAB and the anionic surfactant sodium dodecyl sulfate (SDS). Fig. 3a shows a low-magnification scanning electron microscopy (SEM) image of the PbS product, which exhibits uniform star-like nanocrystals exclusively. An enlarged SEM image shown in Fig. 3b suggests that the stars exhibit a well-defined star-shaped geometry with 6 symmetric horns and the crystal size determined from the distance between two neighboring vertices is ~90 nm. The corresponding TEM image (Fig. 3c) clearly shows a 2D projection of the 3D 6-horn stars, indicating a regular deposition of most stars on the copper grid with 3 horns stably standing on the substrate. The crystal size determined from the distance between every two tips is ~90 nm, in good agreement with crystal size measured from the SEM image. The ED pattern related with a single star shows diffraction spots due to the [1 1 1] zone axis of cubic PbS, indicating that the 6-horn star is actually a PbS single crystal with 6 horns along the ⟨1 0 0⟩ directions. The single-crystallinity of the stars is further confirmed by the HRTEM image shown in Fig. 3d, which was taken from a [1 1 0]-projected star with two horns standing on the substrate by chance, indicating the ⟨1 0 0⟩ direction of each horn. This result provides a useful model system for investigating shape-dependent optical properties of semiconductor nanocrystals and may open a new avenue towards the green chemical synthesis of shape-controlled nanocrystals.

PbS octahedra (~70 nm) were obtained in the presence of 5.7 mM CTAB whereas dendritic PbS crystals partly preserving the hierarchical structure of the original 8-arm stars were produced in the presence of 1.1 mM SDS. These results indicated that the presence of SDS would considerably accelerate the growth on the {1 0 0} faces relative to the {1 1 1} faces leading to the formation of hexapods showing 6 ⟨1 0 0⟩-oriented arms whereas the presence of CTAB tends to just bring about a mild increase in the growth rate on the {1 0 0} faces relative to the {1 1 1} faces, which favors the formation of octahedrons showing 8 {1 1 1} faces. As a result, the presence

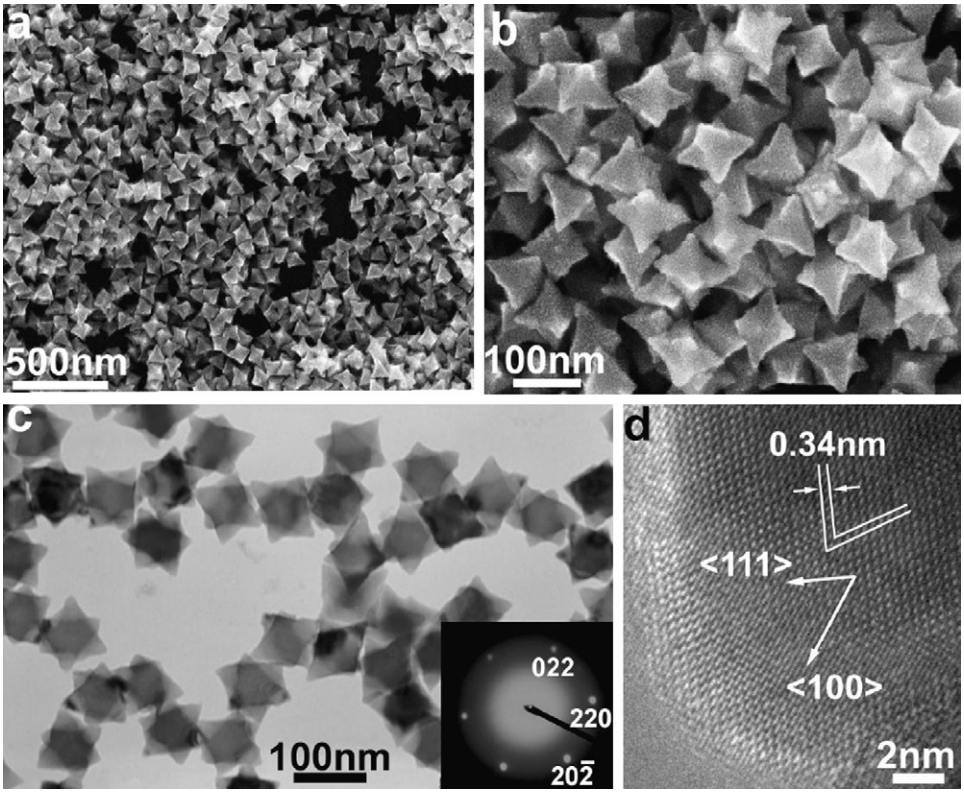

Fig. 3. SEM (a and b), TEM (c) and HRTEM (d) images of star-shaped PbS nanocrystals obtained in mixed CTAB-SDS solution. Inset shows the ED pattern related with an individual PbS star.
Reprinted with permission from Ref. [49]. Copyright 2006 Wiley-VCH.

of the binary CTAB-SDS mixture would lead to the formation of star-shaped PbS nanocrystals as an intermediate morphology between hexapods with 6 ⟨1 0 0⟩-oriented arms and octahedrons with 8 {1 1 1} faces due to a cooperative effect of CTAB and SDS. Hence, the mixed CTAB-SDS surfactants may play the role of binary capping agents in the nucleation and growth of PbS crystals, leading to the gradual growth of star-shaped PbS nanocrystals during the early stages when there is a high monomer concentration, which is favorable for anisotropic crystal growth.

Gold nanostructures have been the focus of intense research owing to their fascinating optical, electronic, and chemical properties and promising applications in nanoelectronics, biomedicine, sensing, and catalysis. Since the shape of gold nanostructures considerably influences their intrinsic properties and relevant applications, great effort has been devoted to the morphology-controlled synthesis of gold nanostructures in recent years. In aqueous solutions of catanionic normal micelles, single-crystalline gold nanobelts and unique gold nanocombs can be readily synthesized. The synthesis of the gold nanobelt-based nanostructures was simply achieved by the reduction of $HAuCl_4$ with ascorbic acid in aqueous solutions of the cationic surfactant CTAB and the anionic surfactant sodium dodecyl sulfonate (SDSn) [50]. Fig. 4a shows a representative SEM image of the gold product obtained at 4 °C, which suggest that the product exclusively consists of very flexible, 1D belt-like nanostructures typically several tens of micrometers in length, ranging from 40 to 150 nm in width, and about 15–20 nm in thickness. Fig. 4b shows a typical TEM image of an individual nanobelt as well as the related ED pattern, which indicates that the whole Au nanobelt is a single crystal grown along the ⟨1 1 0⟩ direction with the top surface of the {1 1 1} plane. While the ⟨1 1 0⟩ direction is the predominant growth direction for the gold nanobelts obtained at 4 °C, the ⟨2 1 1⟩ direction turns out to be the exclusive growth direction for the gold nanobelts obtained at 27 °C. As shown in Fig. 4c, gold nanobelts ranging from 40 to 200 nm in width and about 20–30 nm in thickness were produced. Fig. 4d presents a typical TEM image of an individual nanobelt as well as the related ED pattern, indicating that the whole Au nanobelt is a single crystal grown along the [2 1 1] direction with the (1 1 1) plane as the top surface.

When the reaction solution was initially kept at 4 °C for 0.5 h and subsequently let to stand at 27 °C for 12 h, unique gold nanocombs made of nanobelts about 20–30 nm in thickness could be obtained in addition to the nested Au nanobelts (Fig. 4e and f). The comb-like nanostructures obtained normally consist of a stem belt typically 3–10 μm in length and numerous lateral belts grown perpendicularly on one side of the stem. The ED pattern of a single nanocomb suggests that the gold nanocomb is actually a single crystal with the stem nanobelt grown along the ⟨1 1 0⟩ direction and the side nanobelts grown along the ⟨2 1 1⟩ direction, which are consistent with the growth directions of Au nanobelts grown at 4 °C and 27 °C, respectively. The obtained gold nanobelts and nanocombs would be ideal candidates for investigating the electrical properties of 1D metal nanostructures with specific growth direction and cross-sectional aspect ratio [34] as well as the novel photonic properties of hierarchical architectures of 1D metal nanostructures as potential plasmonic fibers [35]. Moreover, the unique gold nanocombs showing a cantilever-like structure could find promising applications in biosensing and nanodevices. This synthetic strategy may open a new route for the mild fabrication and hierarchical assembly of metal nanobelts in aqueous solution.

A tentative growth mechanism for the gold nanobelts and nanocombs is illustrated in Scheme 2 [50]. The CTAB-SDSn mixture could strongly adsorb on the {1 1 1} planes of cubic gold at both temperatures; meanwhile, it could less strongly adsorb on the {2 1 1} surfaces at 4 °C and on the {1 1 0} surfaces at 27 °C, leading to the formation of ⟨1 1 0⟩-oriented nanobelts and ⟨2 1 1⟩-

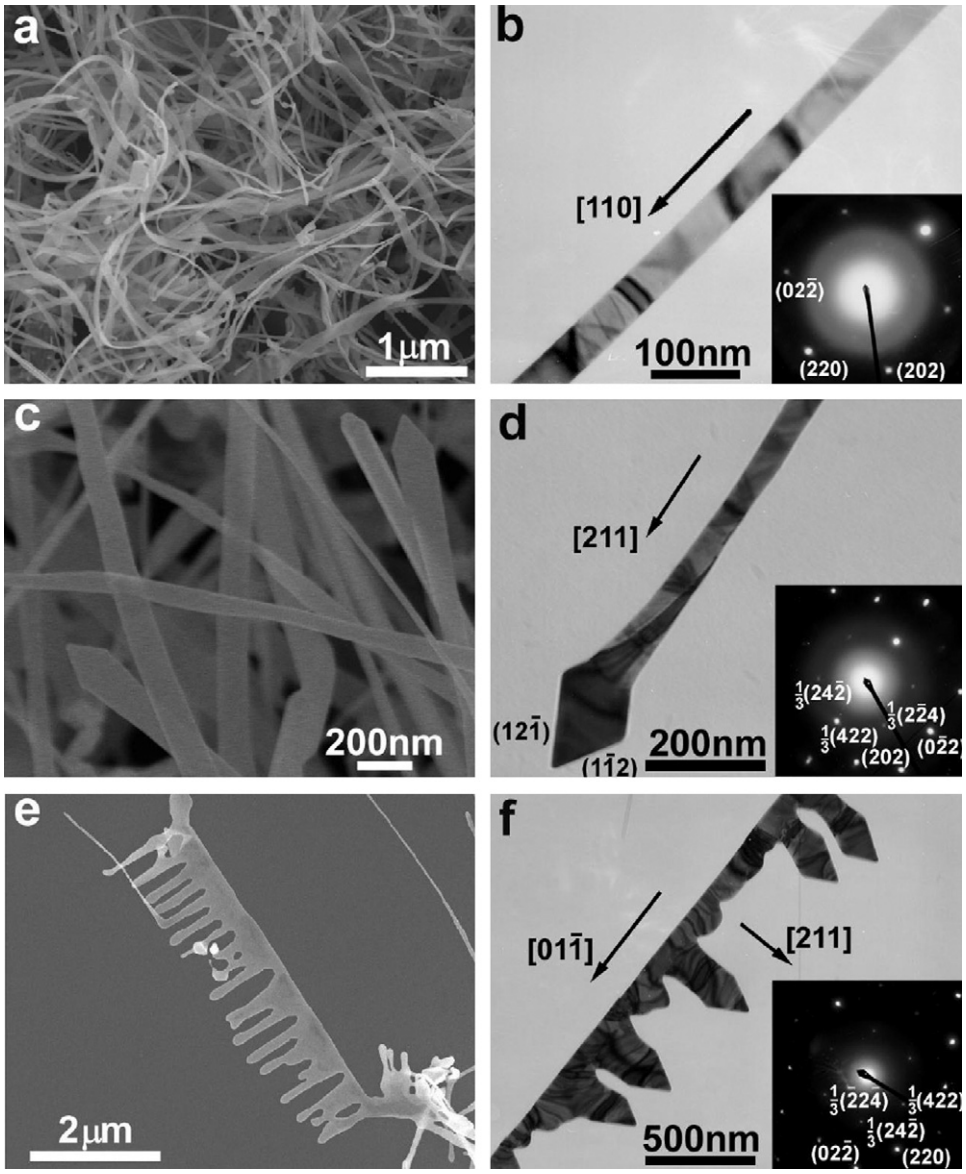

Fig. 4. SEM (a, c, and e) and TEM (b, d, and f) images of gold nanostructures obtained in mixed CTAB-SDSn solutions at 4 °C (a and b), at 27 °C (c and d), and by a two-step process with temperature changing from 4 °C to 27 °C (e and f). Insets show the corresponding ED patterns.
Reprinted with permission from Ref. [50]. Copyright 2008 American Chemical Society.

oriented nanobelts at 4 °C and 27 °C, respectively. The growth of gold nanocombs via a two-step process with temperature changing from 4 °C to 27 °C could be rationalized by considering that the ⟨1 1 0⟩-oriented stem nanobelts formed at 4 °C initially, which was followed by the gradual growth of ⟨2 1 1⟩-oriented lateral nanobelts on one side of the stem. The reason why the lateral nanobelts of the nanocombs just grow along one side remains unclear. A possible explanation could be that one side of the stem nanobelt was tightly adsorbed by the mixed surfactants or approached by the aggregates of the mixed surfactants during the gradual growth of lateral nanobelts on the other side. Such a breaking of symmetry in the crystal growth represents an interesting topic worthy of further study.

The synthesis in aqueous solutions of mixed cationic/anionic surfactants can be extended to the controlled fabrication of other material systems. For example, novel dendritic silver crystals, which consisted of several branches with lengths up to 10 μm, were successfully synthesized by a simple wet chemical route in mixed CTAB and sodium dodecyl benzyl sulfonate (SDBS) surfactant solution at room temperature [51]. The architecture of the silver crystals was drastically influenced by the CTAB/SDBS molar ratio, the surfactant concentration and the precursor concentration. It was revealed that the mixed-surfactant solution might play both capping reagent and dispersion reagent roles. As another example, nanosized SnO_2 with a diversity of different morphologies, such as prism-like, cubic, nanoflower-like, nanosheet-like, was successfully fabricated in mixed CTAB/SDS solutions with different CTAB/SDS molar ratios [52]. The gas sensors constructed by the SnO_2 particles with different morphologies show dramatically different sensor responses to CO and ethanol. In particular, the sensor based on nanoflower-like and mixture of nanoflower-like and prism-like SnO_2 sensors exhibited high sensor response for detecting CO and ethanol, which could be attributed to the formation of a potential barrier at the nanowire/nanowire junctions.

3. Synthesis based on reactive templates

The template method is an effective approach for the controlled synthesis of nanomaterials with both 1D and hollow morphologies and has attracted great effort. A variety of hard templates

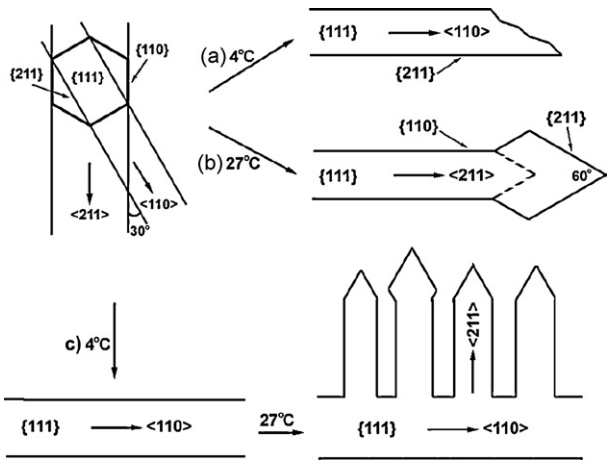

Scheme 2. Schematic illustration of the formation mechanism of gold nanobelts and nanocombs. In the upper left corner is presented a projection perpendicular to the top surface of the {1 1 1} plane including a hexagonal prism to show the relative angles between different growth directions and side faces of the two kinds of nanobelts.
Reprinted with permission from Ref. [50]. Copyright 2008 American Chemical Society.

have been used for this purpose; however, harsh conditions or complicated procedures are generally required to remove hard templates, and the templating effects are not so straightforward in many cases for soft templates. Reactive templates, which act as both templates and reactive precursors or intermediates, are not only free from the template removal problem but also from the limited morphologies of hard templates, because the precursors can be fabricated through all the techniques developed for morphosynthesis of nanomaterials.

3.1. 1D nanostructures

For many kinds of inorganic materials, it is rather difficult to directly fabricate their 1D nanostructures at relatively low temperatures. To circumvent this obstacle, 1D reactive sacrificial templates can be utilized to fabricate 1D inorganic nanostructures with preserved 1D morphologies and desirable compositions through chemical transformation in solution, which provides a straightforward and effective route to fabricate 1D inorganic nanostructures. For example, because of the high reactivity of selenium, trigonal selenium (t-Se) nanowires have been demonstrated to be an effective sacrificial template for the fabrication of a variety of 1D metal chalcogenide nanostructures [53]. Interestingly, long CdTe nanotubes of tunable diameters were synthesized by using diameter-tunable nanowires formed from Cd-TGA coordination polymer and PAA as the 1D sacrificial templates [54]. In a similar way, Zhu et al. reported a novel biomolecule-assisted route to the synthesis of lead chalcogenide polycrystalline nanotubes by templating against precursor nanowires composed of cysteine biomolecules, lead nitrate, and certain amines or ammonia [55].

As a recent example, we successfully synthesized nanofiber bundles of Ag_2S, Ag_2Se, and Ag by using $Ag_2C_2O_4$ nanofiber bundles as 1D reactive template, utilizing both anion-exchange and redox reactions [56]. The obtained Ag_2S, Ag_2Se, and Ag nanofiber bundles were all polycrystalline nanofibers composed of nanoparticles and the precursor morphology was well-preserved, indicating that $Ag_2C_2O_4$ nanofiber bundles acted as a general sacrificial template for the synthesis of silver-based semiconductor and metal nanofibers. Moreover, an electrical transportation and switching device was built with the synthesized nanofiber bundles of Ag_2S and Ag, showing potential applications in nanoscale device building and integration.

Furthermore, we developed a facile and effective method to realize the transformation from t-Se nanotubes to PbSe nanotubes (Scheme 3) [57]. Firstly, single-crystalline t-Se nanotubes with pseudo-hexagonal cross-sections were synthesized in large scale in micellar solutions of a nonionic surfactant [58]. Then, PbSe nanotubes with pseudo-hexagonal cross-sections were prepared by solvothermal transformation of the well-faceted t-Se nanotubes in the presence of $Pb(Ac)_2$ and ascorbic acid in ethylene glycol at 200 °C. Moreover, novel Se@PbSe composite nanotubes consisting of Se nanotubes covered with a PbSe sheath were obtained by shortening the reaction time. Subsequent removal of the inner Se nanotubes resulted in the formation of thin-walled PbSe nanotubes (less than 20 nm in wall thickness). Preliminary electrochemical measurements showed that the prepared PbSe nanotubes exhibited a good electrochemical activity. This solvothermal transformation method provided a simple and effective route to fabricate PbSe nanotubes with adjustable wall thicknesses and Se@PbSe composite nanotubes with tunable compositions, which would find potential applications including nanodevice fabrication.

Recently, SnO_2 nanotubes with controllable morphologies have been successfully synthesized by using a variety of 1D silica mesostructures as effective reactive templates (Fig. 5) [59]. Firstly, 1D silica mesostructures with different morphologies, such as chiral nanorods, nonchiral nanofibers and helical nanotubes, were readily synthesized in aqueous solution by using the triblock copolymer Pluronic F127 and the cationic surfactant CTAB as binary templates. Subsequently, the obtained 1D silica mesostructures were used as sacrificial templates to synthesize SnO_2 nanotubes with preserved morphologies via a simple hydrothermal route, resulting in the formation of well-defined SnO_2 nanotubes with different lengths and unique helical SnO_2 nanotubes with a wealth of conformations. It was revealed that both of the short and long SnO_2 nanotubes showed much better performance as anode materials in lithium ion batteries than normal SnO_2 nanopowders, which might be related to the hollow structure of the nanotubes that could alleviate the volume changes and mechanical stress during charging/discharging cycling. Moreover, the capacity and cycling performance of short nanotubes, which showed a specific discharge capacity of 468 mAh g^{-1} after 30 cycles, were considerably better

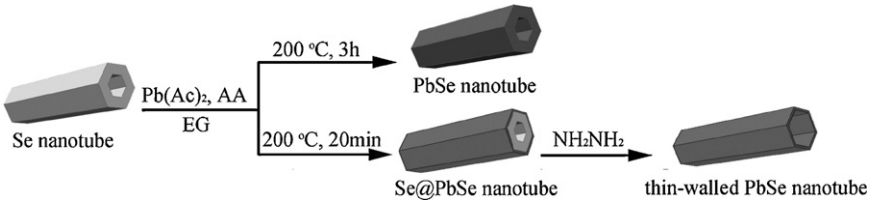

Scheme 3. Schematic illustration of a possible mechanism for the template-directed formation of PbSe nanotubes with different wall thicknesses and Se@PbSe composite nanotubes.
Reprinted with permission from Ref. [57]. Copyright 2009 IOP Publishing Ltd.

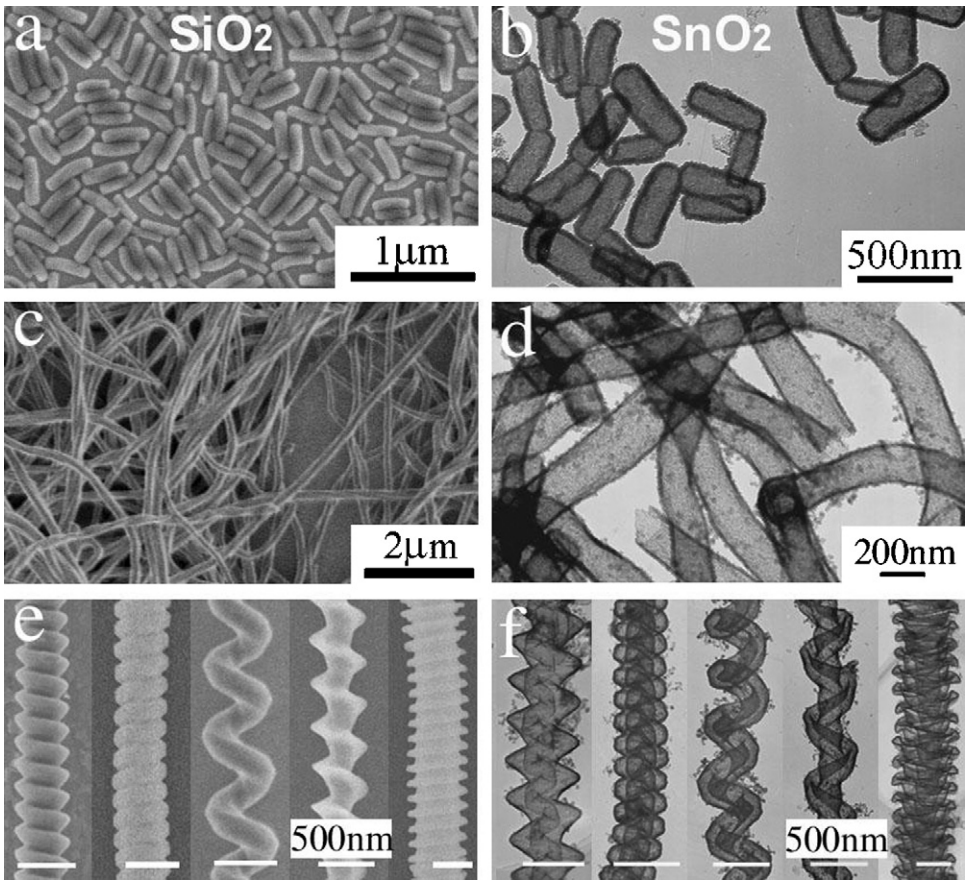

Fig. 5. SEM images of mesostructured silica chiral nanorods (a), nonchiral nanofibers (c), and helical nanofibers (e) and TEM images of the templated SnO_2 short nanotubes (b), long nanotubes (d), and helical nanotubes (f).
Reprinted with permission from Ref. [59]. Copyright 2010 Wiley-VCH.

than those of long nanotubes because of the more robust structure of the short nanotubes.

The controlled synthesis of 1D nanostructures and guiding them to ordered superstructures or complex functional architectures would offer great opportunities to explore their novel properties and to fabricate useful nanodevices. In this regard, it remains a great challenge to develop rational synthetic methods to fabricate complex nanorod/nanowire superstructures with desired architectures. Recently, we developed a novel 2D-template-engaged topotactic reaction method to synthesize hierarchical disc-like Bi_2S_3 networks composed of perpendicularly aligned single-crystalline nanorods [60]. Fig. 6 presents typical SEM and TEM images of the Bi_2S_3 networks obtained after reacting the BiOCl precursor discs with TAA. It was revealed that these superstructures were formed by the preferential growth of [0 0 1]-oriented Bi_2S_3 nanorods on the top faces of (0 0 1)-oriented BiOCl discs along the two perpendicular [1 0 0] and [0 1 0] directions of BiOCl.

The structural relationship between the *c* axis of orthorhombic Bi_2S_3 ($c = 3.98$ Å) and the *a* or *b* axis of tetragonal BiOCl ($a = b = 3.89$ Å) could be responsible for the topotactic transformation from a single-crystalline disc-like template to a disc-like nanorod networks (Scheme 4) [60]. When the sulfur ions released from TAA diffused to the top surfaces of BiOCl single-crystalline discs with the top faces of the (0 0 1) plane, the sulfur ions might replace the oxygen ions and chlorine ions to generate [0 0 1]-oriented Bi_2S_3 single-crystalline nanorods lying on the top surfaces due to the lower solubility of Bi_2S_3. Moreover, these [0 0 1]-oriented Bi_2S_3 single-crystalline nanorods would tend to orient along the two perpendicular [1 0 0] and [0 1 0] directions of BiOCl due to the close lattice matching between the *c* axis of Bi_2S_3 and the *a* or *b* axis of BiOCl, leading to the formation of a layer of disc-like network consisting of crossed nanorods on the top faces of BiOCl discs. The close lattice matching indicates a minimal reorganization of structure in the precursor solid, which could be the key to the formation of single-crystalline products from a single-crystalline template. Namely, the lattice constant of the *a* or *b* axis of BiOCl was essentially unchanged during the formation of [0 0 1]-oriented Bi_2S_3 single-crystalline nanorods upon topotactic transformation from the 2D precursor template. To the best of our knowledge, this work represents the first topotactic transformation process capable of generating 2D networks consisting of single-crystalline nanorods. This approach is potentially extendable to the fabrication of 2D networks made of 1D single-crystalline nanostructures with desirable properties and could open new avenues for the bottom-up fabrication of nanodevices assembled from 1D nanostructures.

3.2. Hollow structures

The synthesis via reactive templates has remarkable advantages in the large-yield preparation of hollow structures with designed sizes, nonspherical shapes, and hierarchical architectures. These chemical processes include the Kirkendall effect, galvanic replacement, oxidative evacuation, etc. Among them, the sacrificial template-directed chemical transformation method based on the Kirkendall effect has been demonstrated to be an effective approach [61]. The Kirkendall effect is the mutual diffusion rates of two components in a diffusion couple differ by a considerable amount so that vacancy diffusion occurs to compensate for the inequality of the material flow and the initial interface moves. The physical phenomenon may provide possibilities for fabrication of new nano-

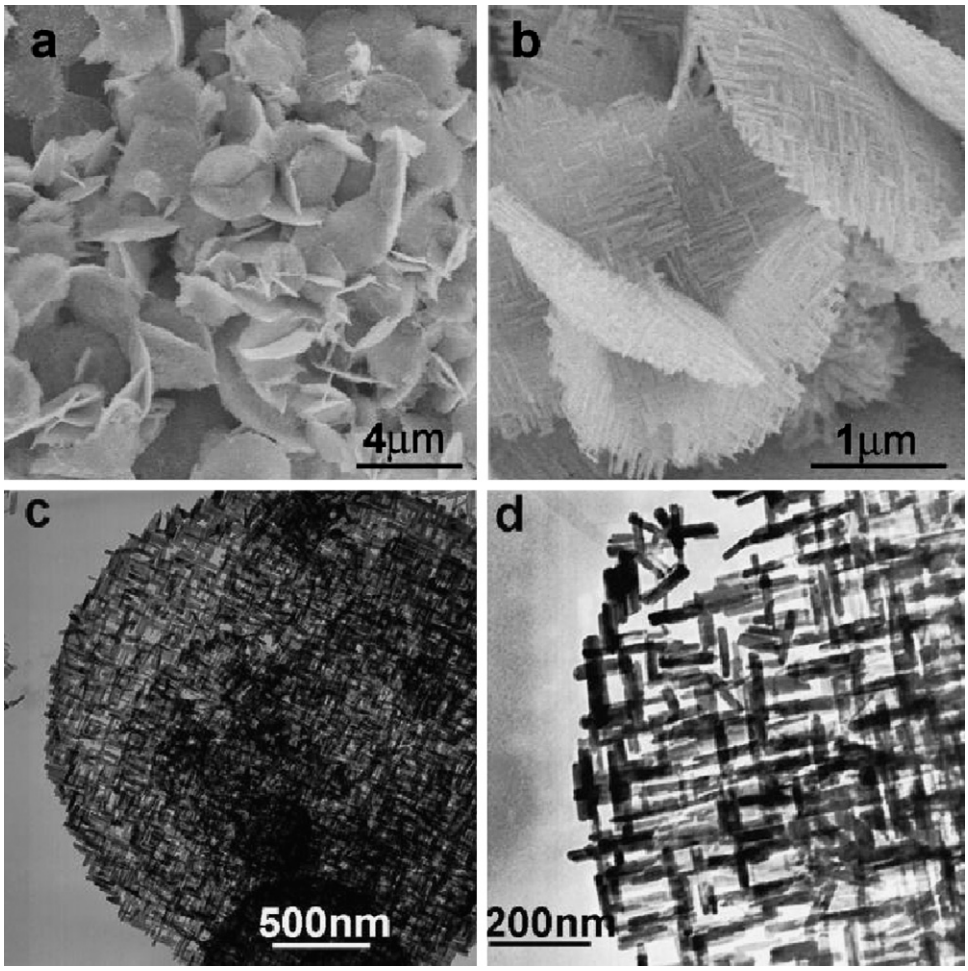

Fig. 6. SEM (a and b) and TEM (c and d) images of disc-like Bi_2S_3 nanorod networks obtained by transformation of BiOCl discs. Reprinted with permission from Ref. [60]. Copyright 2008 Wiley-VCH.

materials with hollow interiors considering the directional matter flow and consequential vacancy accumulation in Kirkendall type diffusion.

We successfully prepared uniform copper sulfide and oxide hollow spheres by using reactive templates based on the Kirkendall effect [62]. The in situ formed sacrificial template containing Cu(I) can be employed as a general reactive template for the fabrication of hollow microspheres of Cu_2O and CuS. The shell thickness of these hollow spheres can be adjusted through the choice of the bromide source used for the formation of intermediate templates. Uniform thick-shell CuS hollow spheres with a shell thickness of about 130–180 nm (Fig. 7a and b) were obtained by using CuBr solid spheres as the templates, which were formed by the reduction of $CuBr_2$ with ascorbic acid. On the other hand, uniform thin-shell CuS hollow spheres a shell thickness of about 20–25 nm (Fig. 7c and d) were readily obtained if Cu(I)-containing aggregates instead of CuBr solid spheres were employed as the template. In this case, $(C_4H_9)_4NBr$ and $CuCl_2$ were used as the bromide and copper sources, respectively, rather than the use of $CuBr_2$ as both the bromide and copper sources. The shell thickness of the hollow spheres could be related to the content of Cu(I) ions in the spherical templates. Namely, a relatively smaller content of Cu(I) ions in the loose aggregates would result in a much thinner shell for the final hollow spheres. It was also revealed that these CuS hollow spheres exhibited remarkable optical limiting effects, which could make them useful for protecting human eyes or optical sensors from high-power laser irradiation. In a similar way, hierarchical, core–shell structured microspheres of a series of bismuth chalcogenides were synthesized by chemical transformation of intermediate BiOCl microspheres [63]. The photoresponsive properties of the obtained hierarchical Bi_2S_3 core–shell microspheres were investigated, which showed better sensitivity than normal Bi_2S_3 nanorods probably owing to multiple reflections of light within the sphere interior voids.

The reactive templates can be extended to the synthesis of nonspherical hollow structures. In particular, we obtained hierarchical assembly of rhombododecahedral silver cages through the microscale Kirkendall effect by employing rhombododecahedral Ag_3PO_4 crystals as reactive precursor templates [64]. Ag_3PO_4 crystals with uniform rhombododecahedral morphology (Fig. 8a and b) were used as reactive precursor template for the morphology-preserved synthesis of silver particles using different reducing agents. Fig. 8c and d shows the SEM image of single-walled Ag rhombododecahedral cages obtained by the reduction of the precursor crystals in ascorbic acid solution, which suggests the formation of hollow silver particles with a well-preserved rhombododecahedral morphology. Hydrazine is a stronger reductant and has a higher diffusion ability than ascorbic acid, and unique double-walled Ag cages with rhombododecahedral morphology can be obtained when hydrazine is used as reductant instead of ascorbic acid (Fig. 8e). The double-walled pattern is reminiscent of the well-known Liesegang patterns that typically form by a periodic precipitation through the moving reaction front when two coprecipitating reactants interdiffuse in a gel medium. If $NaBH_4$,

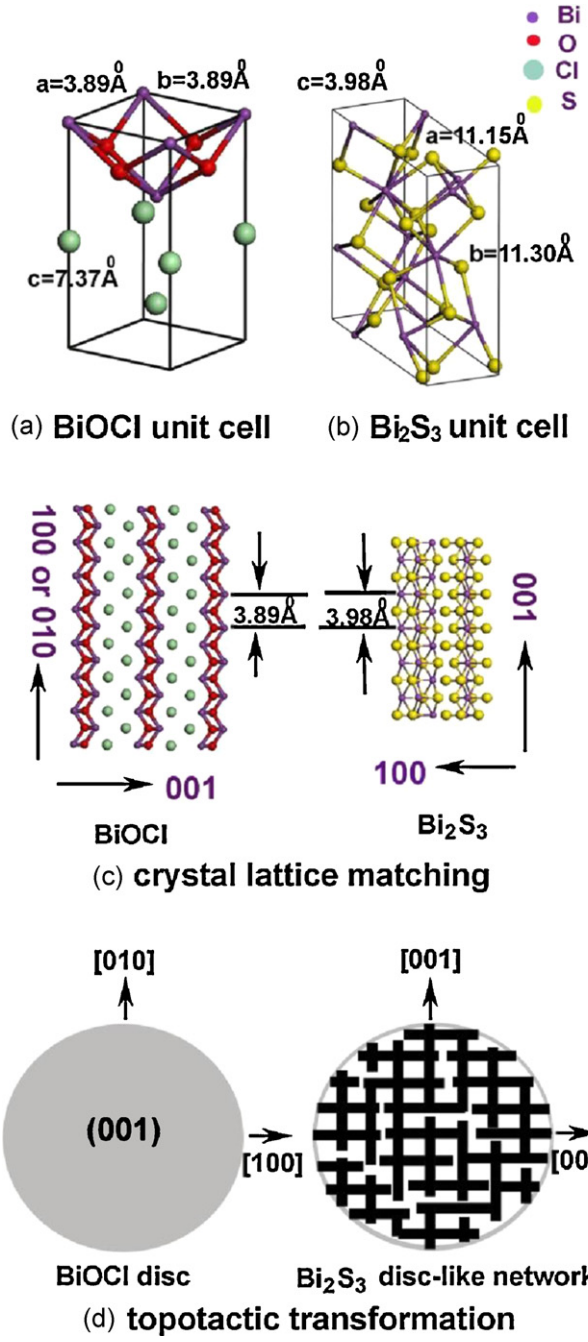

Scheme 4. Schematic illustration of (a) tetragonal BiOCl unit cell, (b) orthorhombic Bi_2S_3 unit cell, (c) the crystal lattice matching between tetragonal BiOCl and orthorhombic Bi_2S_3, and (d) the topotactic transformation from BiOCl disc to Bi_2S_3 disc-like network.
Reprinted with permission from Ref. [60]. Copyright 2008 Wiley-VCH.

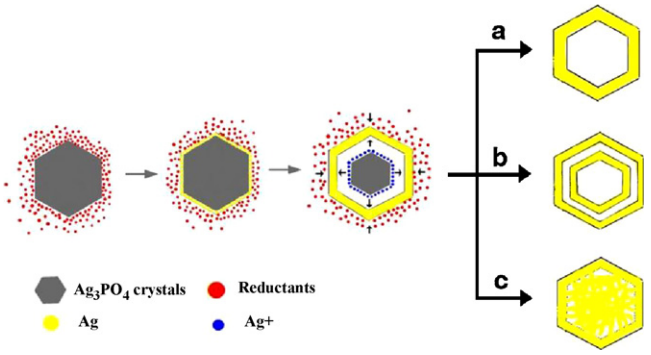

Scheme 5. Schematic illustration of the formation of hierarchical, silver rhombdodecahedral particles: (a) single-walled cages, (b) double-walled cages, and (c) core–shell structured particles.
Reprinted with permission from Ref. [64]. Copyright 2005 Wiley-VCH.

which has an even higher reducing ability and diffusion ability, is used as the reducing agent, novel core–shell structured silver rhombododecahedra are produced (Fig. 8f).

A tentative mechanism was proposed for the formation of the three different types of silver rhombododecahedra (Scheme 5) [64]. Briefly, a layer of interconnected silver networks formed around the exterior surface of the Ag_3PO_4 rhombododecahedra as long as they were surrounded by a sufficient concentration of the reductant. Then, the network layer developed into a denser shell, which was accompanied by the formation of a depletion layer near the shell as a result of the coupled reaction/diffusion process. The final silver structure was dependent on the inward diffusion rate of the reductant relative to the outward diffusion rate of the Ag^+ ions, namely, single-walled rhombododecahedra formed with ascorbic acid, which had a low diffusion rate, whereas double-walled rhombododecahedra formed with hydrazine, which had a medium diffusion rate, and core–shell structured rhombododecahedra formed with $NaBH_4$, which had a high diffusion rate. The controlled self-assembly of silver particles produced in situ around the precursor crystal surfaces led to the formation of morphology-preserved, single- or double-walled silver cages constructed from different building units, such as particles, nanoplates, and quasispherical assemblies of nanoplates. This process provided a general route to the synthesis of silver superstructures with unique morphologies and complex hierarchies. Furthermore, this strategy could be extended to other metal systems and could possibly be used for device fabrication with appropriate metal/precursor/reductant combinations.

Another example for the synthesis of nonspherical hollow structure through reactive templates is the fabrication of octahedral Cu_2O nanocages by a catalytic solution route, which involved the formation of octahedral Cu_2O nanocrystals and a subsequent spontaneous hollowing process through oxidative evacuation [65]. In this synthesis, $PdCl_2$ was introduced into the reaction mixture of Fehling's solution (copper tartrate complex) and the reductant glucose for the catalytic solution synthesis of unique octahedral Cu_2O nanocages. A typical SEM image of the Cu_2O crystals obtained after 3 h of aging at 75 °C is shown in Fig. 9a, which suggests that the product exhibits uniform, regular octahedral with an average edge length of 230 nm. The well-defined octahedral morphology with a cubic symmetry is characteristic of single-crystalline cubic-structured Cu_2O crystals bound by eight planes (Fig. 9b). Fig. 9c shows a typical TEM image of the Cu_2O product, which suggests that the octahedral particles are actually octahedral nanocages with a wall thickness typically in the 10–14 nm range. The selected area electron diffraction (SAED) pattern corresponding to a single nanocage showing a rhombic projection can be indexed to the [1 1 0] zone axis of cubic-structured Cu_2O with a [0 0 1] direction along the longer diagonal direction of the rhomb. The single-crystalline nature of the nanocages has been further demonstrated by the HRTEM image shown in Fig. 9d, which exhibits clear fringes attributed to the (1 1 0) planes of Cu_2O. A wealthy of colorful Cu_2O nanostructures with widely tunable bandgaps in the range of 2.6–2.2 eV have been obtained by this synthetic route. This facile one-pot approach to inorganic hollow structures with novel morphologies could be potentially extended to other inorganic systems.

It is worth noting that several other research groups have made great contributions to the fabrication of nonspherical hollow

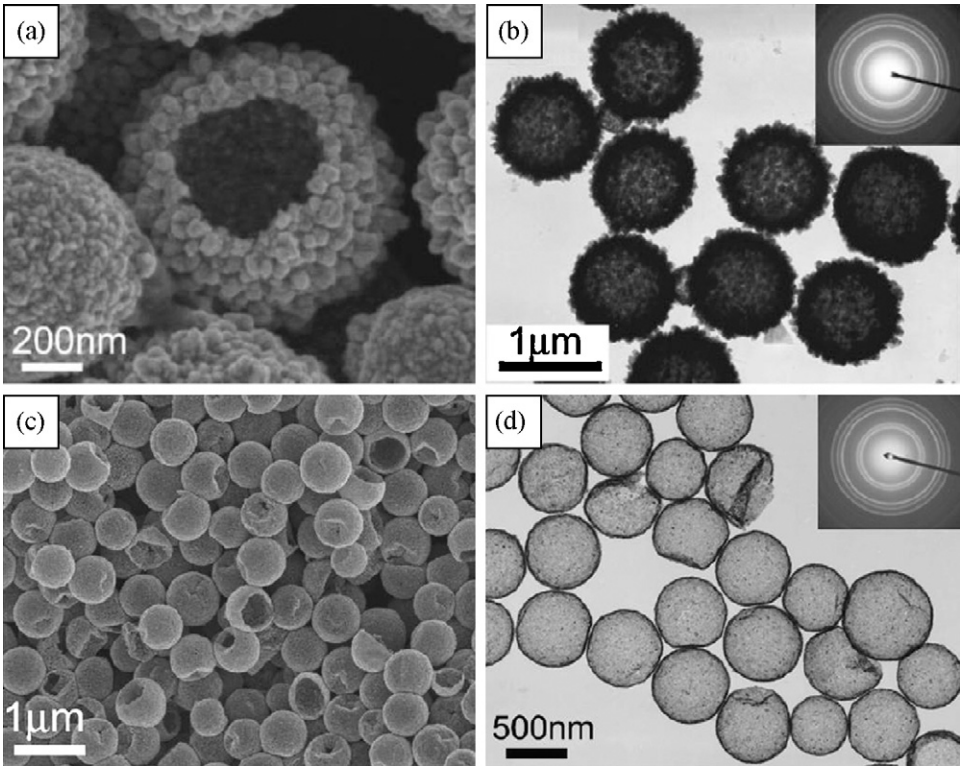

Fig. 7. SEM (a and c) and TEM (b and d) images of thick-shell (a and b) and thin-shell (c and d) CuS hollow spheres obtained via reactive templates. Insets show the corresponding ED patterns.
Reprinted with permission from Ref. [62]. Copyright 2008 American Chemical Society.

structures by using shape-controlled solid precursors as reactive templates. For example, Qian and co-workers successfully synthesized high symmetric 18-facet polyhedron nanocrystals of Cu_7S_4 with a hollow nanocage through the chemical transformation of truncated cubic Cu_2O nanocrystals [66]. Xu and co-workers prepared well-defined nonspherical copper sulfide mesocages with single-crystalline shells by shape-controlled Cu_2O crystal templating [67]. Xie and co-workers synthesized micrometer scaled MoS_2 hierarchical hollow cubic cages assembled by bilayers via a one-step self-assembly coupled with intermediate crystal templating process, in which the intermediate $K_2NaMoO_3F_3$ crystal formed in-situ and then served as the self-sacrificed template based on the Kirkendall effect [68]. Li and co-workers reported the synthesis of hierarchical hollow MnO_2 microcubes by shape-preserving oxidation of $MnCO_3$ microcubes [69]. Recently, Yu and co-workers described the hydrothermal synthesis novel anatase TiO_2 boxes by using rectangular particulates with a composition of $(TiO_2)_2{\cdot}C_4H_6O_5{\cdot}6H_2O$ as reactive templates [70].

4. Synthesis based on colloidal crystal templates

Colloidal crystals are generally two- or three-dimensionally close-packed arrays of monodisperse colloidal particles. The long-range ordered structures possessed by colloidal crystals have made them of great interest in several research aspects of advanced materials. The periodic alternation in dielectric constant on the length scale of submicrometer endows colloidal crystals with promising application as bottom-up self-assembled photonic band gap (PBG) materials. Another promising application of colloidal crystals is their use as hard templates for the fabrication of inversely replicated functional materials such as three-dimensionally ordered macroporous (3DOM) materials [27,28], and as lithographic mask for the fabrication of 2D ordered nanoarrays or nanoporous thin films through the nanosphere lithography (NSL) technique [31,71,72].

4.1. 3DOM single crystals

The direct fabrication of single crystals with patterns on the micro- and nanometer length scale is of great technological significance, as these patterned structures are constituent parts in the construction of devices used in electronics, optics and sensor [73]. Particularly, single crystals with 3D ordered macropores might be promising candidates for highly desirable photonic crystals with full photonic band gaps and birefringent photonic crystals with optical tunability due to their anisotropic refractivity [74,75]. However, the 3DOM materials prepared are mostly polycrystalline or amorphous because it is very difficult to maintain the complex structural features on the micro- and nanometer scale without losing the single-crystalline nature [27]. On the other hand, organisms have provided us with excellent examples of beautifully sculpted single crystals, for example, the calcite skeletal plates of echinoderms and coccoliths. Inspired by the biomineralization principles, Aizenberg et al. succeeded in fabricating large-area micropatterned calcite single crystals by controlling the crystallization of the pre-molded ACC precursor [76]. Nevertheless, the experimental procedure was relatively complex and only 2D patterns on the length scale of tens of micrometers were incorporated into the as-obtained single crystals.

Recently, we developed a facile, bioinspired strategy to create 3DOM calcite single crystals, which was achieved by infiltration of freshly prepared transient ACC dispersions into colloidal crystals templates with the assistance of vacuum suction [77]. The transient ACC was prepared by rapidly mixing solutions containing calcium and carbonate ions without the presence of any organic stabilizers. The liquid ACC granules would solidify and crystallize

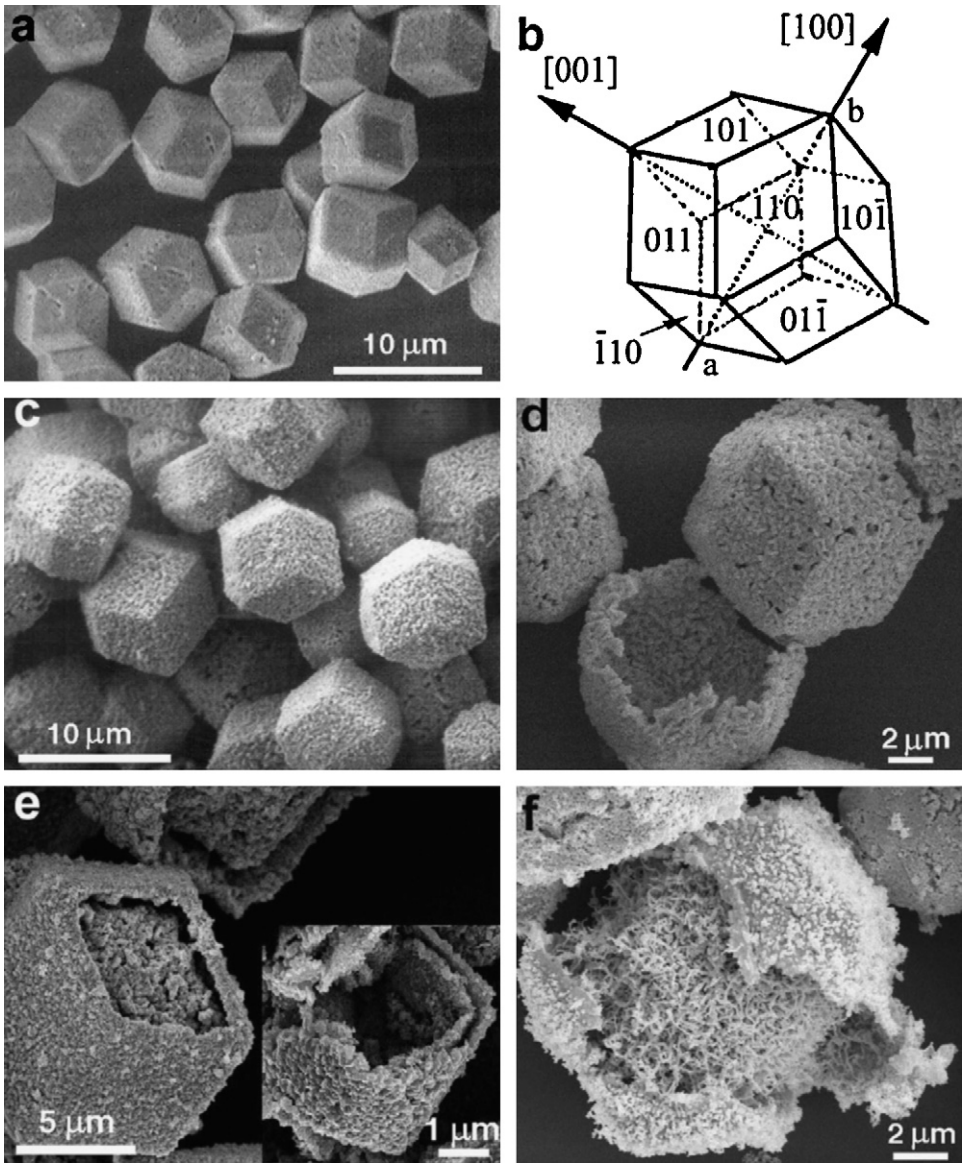

Fig. 8. (a) SEM image of Ag_3PO_4 rhombododecahedral crystals employed as reactive templates and (b) index of a Ag_3PO_4 rhombododecahedral crystal model. (c–f) SEM images of silver rhombododecahedral particles obtained by using different reducing agents: (c and d) single-walled Ag cages produced with ascorbic acid, (e) double-walled Ag cages produced with hydrazine, and (f) Ag core–shell structured particles produced with $NaBH_4$.
Reprinted with permission from Ref. [64]. Copyright 2005 Wiley-VCH.

into a single crystal soon after their infiltration through the interstices of the colloidal crystal template. The applied vacuum suction during the infiltration of ACC guaranteed the rapid feeding of the transient phase to crystallization sites, thus avoiding direct nucleation on the top surface of the template. Carboxylate groups of the poly(styrene-methyl methacrylate-acrylic acid) colloidal crystal template provided strong affinity to the ACC phase and hence enhanced the interstice filling of ACC.

Fig. 10 shows typical SEM images of the obtained 3DOM calcite single crystals. A top view shown in Fig. 10a exhibits a flat, dendritic morphology with two pronounced backbones perpendicular to each other and larger than 50 μm in length. A rhombohedral core lies at the intersection of the two crossed backbones with the two diagonals of the top rhombus just along the two backbones. An enlarged image shown in Fig. 10b revealed an interconnected network of spherical voids imprinted in the crystal, inheriting the hexagonal-close-packed (hcp) order of the colloidal crystal template. Some small ridges protrude on the flat surface, reflecting the dendritic characteristic of the whole crystal. Fig. 10c presents a typical opposite view of the obtained flat dendritic crystals, which shows that the central part is considerably thicker than the peripheral regions. An enlarged image shown in Fig. 10d clearly shows that the crystal is entirely perforated. A high-magnification image (Fig. 10e) exhibits the well-defined, 3D ordered macropores with a pore size of ~445 nm, slightly smaller than the original colloidal spheres. A side view of the crystal (Fig. 10f) suggests that the relatively thinner peripheral region with the 3DOM structure has a thickness about 2 μm. Namely, at least ~5 layers of the colloidal spheres were replicated by the flat calcite crystal at the peripheral regions. While the calcite crystal was thoroughly perforated by 3D interconnected ordered macropores, it turned out to be single-crystalline as demonstrated by the corresponding electron diffraction and polarized light microscopy characterizations.

Scheme 6 illustrates a possible formation process of the 3DOM calcite single crystals on the basis of the experimental observations [77]. The molded ACC went through a single nucleation process initiated by an evolving rhombohedral-shaped calcite core formed from an initial amorphous “tuber”. Subsequent growth

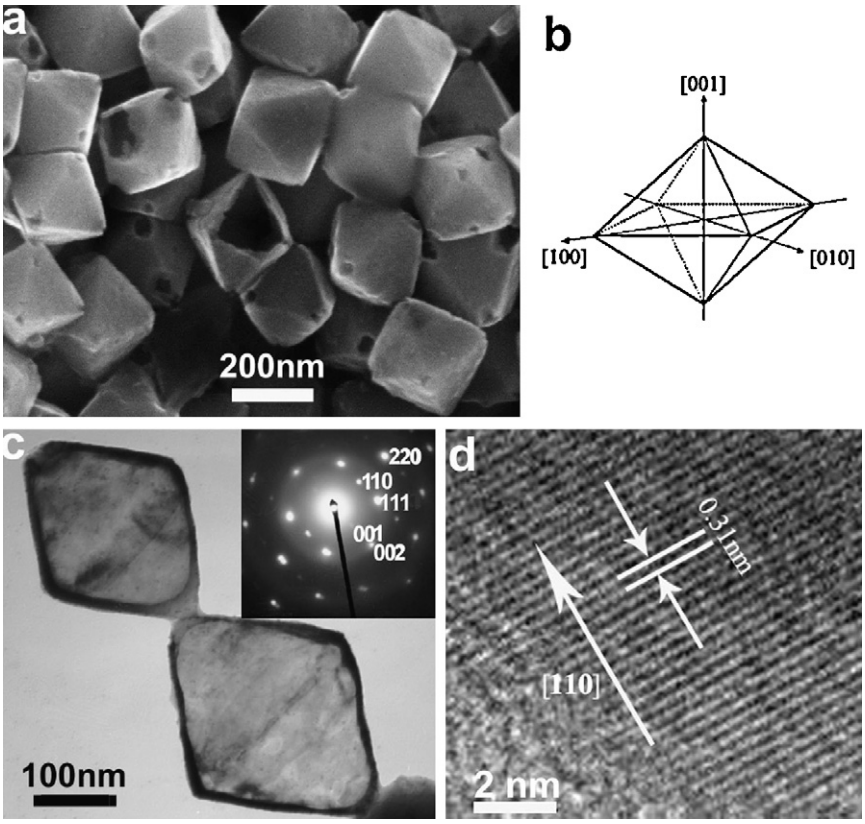

Fig. 9. SEM (a), TEM (c) and HRTEM (d) image of octahedral Cu_2O nanocages obtained by a catalytic etching route. (b) Schematic illustration of an octahedral Cu_2O crystal. Inset to (c) shows the ED pattern of the upper Cu_2O nanocage.
Reprinted with permission from Ref. [65]. Copyright 2005 Wiley-VCH.

at the expense of ACC under non-equilibrium conditions led to its lateral expansion into dendritic crystal while retaining the crystallographic orientation. Accidentally, this nucleation and crystallization process resembles the initial formation process of the sea urchin larval spicule. Our approach may be a significant step towards large 3DOM single crystals since it combines several desirable features of an easy and versatile synthesis via amorphous precursor particles. Since colloidal crystals represent a topologically complex confinement with a resolution at the nanometer scale, this approach may represent a general strategy for the design and fabrication of functional single-crystalline materials with desired nanopatterns, orientations and shapes. For example, this approach could be applied to other nanopatterned templates to obtain calcite single crystals patterned with even smaller features, which has been recently demonstrated [78].

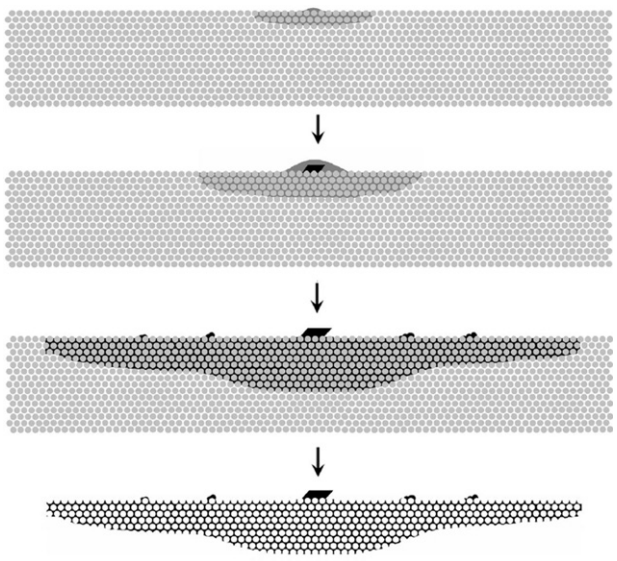

Scheme 6. Schematic illustration of the formation process of flat 3DOM calcite single crystals.
Reprinted with permission from Ref. [77]. Copyright 2008 Wiley-VCH.

The amorphous precursor pathway was crucial for the formation of 3DOM calcite single crystal in this approach. It has been pointed out that the application of amorphous precursor phases for the infiltration of an organic template with subsequent crystallization is an important transfer of biomineralization principles into the realm of synthetic materials [79]. Our approach may be a significant step towards large 3DOM single crystals since it combines several desirable features of an easy and versatile synthesis via amorphous precursor particles. However, efficient approaches remain to be developed to obtain larger (macroscopic) 3DOM single crystals with controllable thickness and crystal orientation, which is essential to their application in optical devices.

4.2. 2D nanoarrays and nanonets

Nanosphere lithography, which generally employs monolayer colloidal crystals as the 2D lithographic mask, has been proven to be a flexible and cost-effective technique to fabricate nanostructured arrays with 2D long-range order. In recent years, 1D ZnO nanostructures have stimulated intensive interest because of their unique semiconducting and piezoelectric properties; furthermore, the alignment of these 1D ZnO nanostructures into ordered nanoarrays can bring about improved performance in several promising applications such as UV laser, dye-sensitized

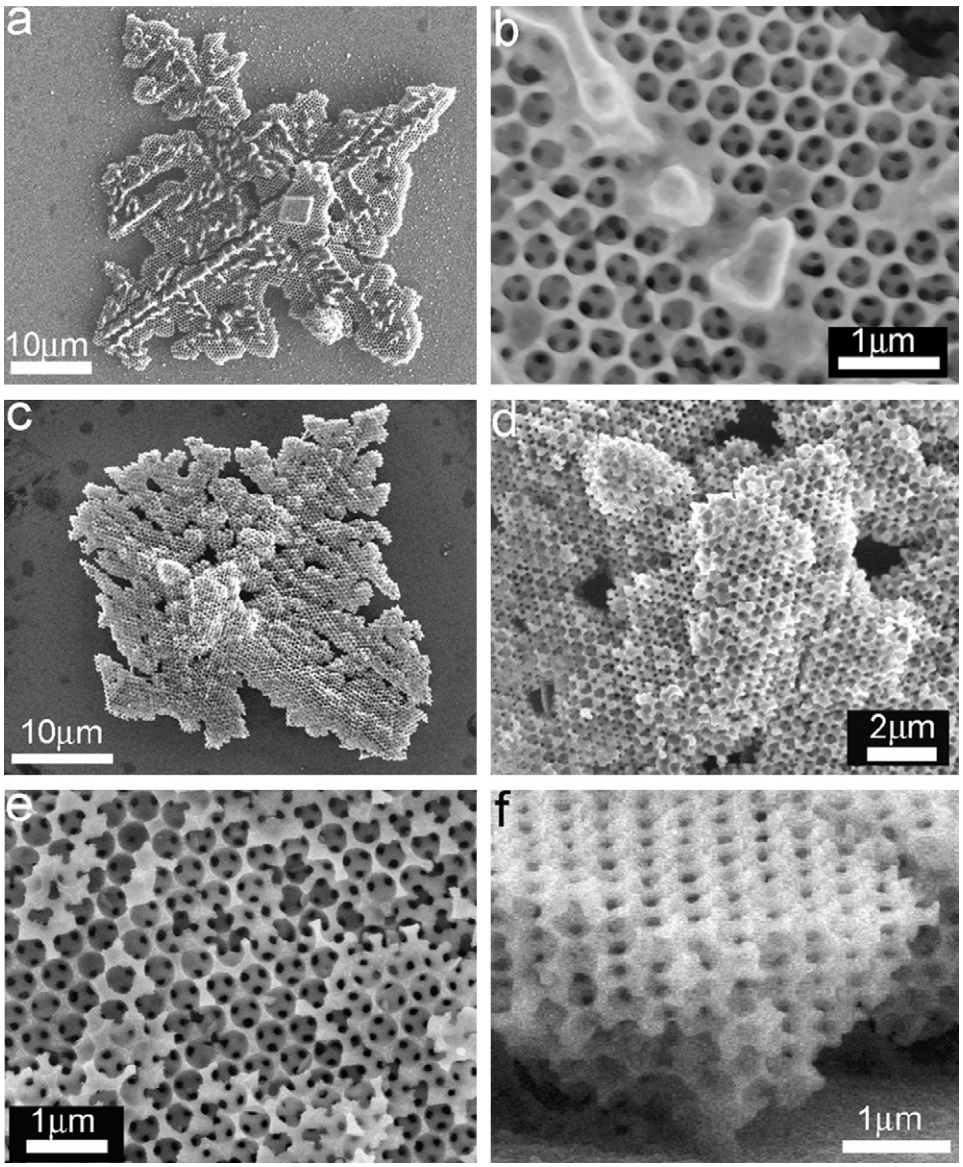

Fig. 10. SEM images of 3DOM calcite single crystals formed by colloidal crystal templating via a transient ACC precursor: (a and b) top view, (c–e) opposite view, and (f) side view.
Reprinted with permission from Ref. [77]. Copyright 2008 Wiley-VCH.

solar cells, piezo-nanogenerators, and antireflection coatings [80]. To integrate devices for such applications it is essential to realize rational control over the pattern (e.g., morphology, diameter, orientation, location and spacing) of the 1D ZnO nanostructure arrays. NSL has turned out to be a useful tool to create metal catalyst nanoarrays on a substrate for the patterned growth of 1D ZnO nanoarrays via vapor phase process. However, it remains a great challenge to develop facile solution routes to the individually patterned growth of well-aligned 1D ZnO nanoarrays with good control over both the pattern and the crystal quality.

We recently demonstrated the fabrication of well-aligned, individually patterned, regular ZnO nanopillar arrays assisted by MCC directly on zinc foil from solution [81]. The experimental process is illustrated in Scheme 7. By either replicating inversely or connecting the pristine monolayer colloidal crystals, two kinds of highly ordered masks were derived from MCC, which were denoted as inverted MCC (IMCC) and connected MCC (CMCC), respectively. Individual ZnO nanopillars grew vertically at each growth site and formed arrays that precisely reserved the hexagonal periodicity of the IMCC and CMCC templates. The diameter of the ZnO nanopillars can be controlled in a wide range from 60 to 900 nm by varying the structural parameters of MCC templates and the growth condition. With the IMCC template, the width and spacing of the ZnO nanopillar arrays can be readily tuned by varying the colloidal sphere size of the MCC template or by elongating the reaction period. Interestingly, the vertically aligned ZnO nanopillars are also side-oriented, indicating a quasi-epitaxial growth on the zinc substrate. The as-integrated ZnO nanopillar arrays showed lower defect density and hence higher optical quality, which promises their potential applications in optical devices such as stimulated emitters and lasing cavities.

On the other hand, nanoholes periodically patterned in a continuous thin film often lead to unusual properties due to scattering of electromagnetic wave on the sub-wavelength scale. Ordered nanonets could also provide useful masks for the fabrication of patterned nanoarrays or novel nanoobjects. Moreover, nano/microsieves with monodisperse pores and high pore density are desirable as high-performance nano/microfiltration mem-

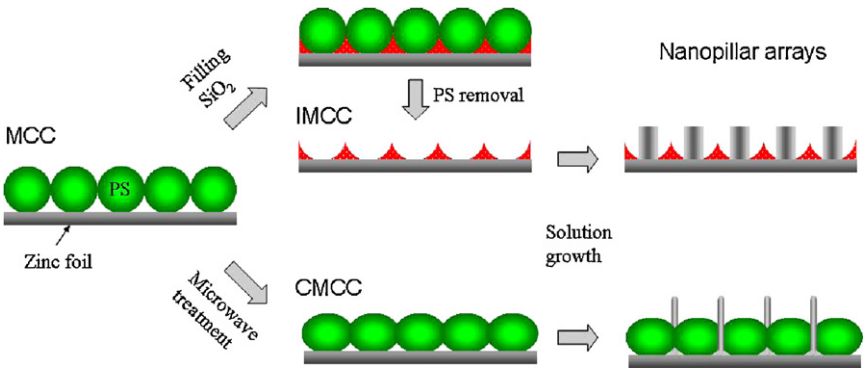

Scheme 7. Schematic illustration of the fabrication process of ZnO nanopillar arrays assisted by monolayer colloidal crystals. Reprinted with permission from Ref. [81]. Copyright 2009 American Chemical Society.

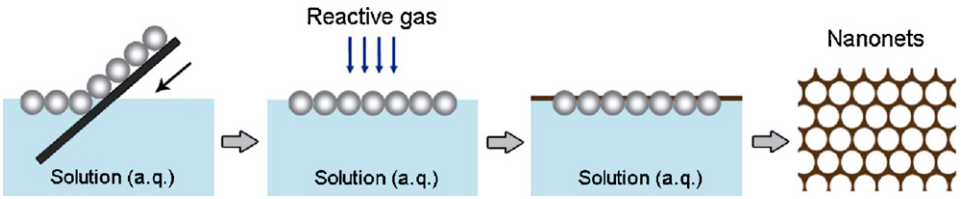

Scheme 8. Schematic illustration of the fabrication of free-standing high-quality nanonets by nanosphere lithography at the gas/liquid interface. Reprinted with permission from Ref. [82]. Copyright 2009 American Chemical Society.

branes. A variety of methods have been developed to fabricate such regular porous membranes; however, of the reported strategies, few combine generality and simplicity for the production of large-area, highly ordered nanonets. Therefore, it remains a great challenge to develop general methods to fabricate high-quality nanonets with both excellent transferability and compositional diversification.

Recently, we developed a very simple and general NSL approach to fabricate large-area free-standing nanonets with high regularity at the gas/liquid interface by using the floating MCC at a solution surface as the mask for the interfacial material deposition via interface reactions [82]. Scheme 8 shows schematically a process flow outlining the major steps leading to the formation of free-standing nanonets. Firstly, an MCC film was assembled on a solid substrate, which was then released onto the reactant solution surface. Secondly, a reactive gas atmosphere was introduced to initiate the interfacial reaction with the subphase. Finally, a sheet of intact nanonet was obtained after a proper period of reaction by dissolving away the MCC mask. The floating state of the nanonets allows their convenient transfer onto any solid substrates. This NSL approach provides a facile total-chemical procedure that is compatible with a variety of materials, such as metal sulfides, metals as well as inorganic minerals, and can be carried out at room temperature without any special equipment. The hole size, spacing, and thickness of the highly ordered nanonets, which showed interesting photonic properties, can be readily adjusted. Furthermore, a variety of ordered gold nanoarrays with unusual patterns were produced by using nanonet bilayers as unique deposition masks, suggesting that the obtained transferable, high-quality nanonets can function as versatile lithographic masks to generate novel nanopatterns.

5. Conclusions and outlook

In the past decade, various colloidal chemical approaches have been successfully developed for synthesizing inorganic micro- and nanostructures with controlled morphologies and patterns. This review summarized our recent research results in the controlled synthesis of inorganic micro- and nanostructures with tailored morphologies and patterns via three typical colloidal chemical routes, i.e., synthesis based on catanionic micelles, reactive templates, and colloidal crystal templates. Catanionic reverse micelles turn out to be effective nanostructured reaction media for the controlled synthesis of 1D nanostructures and their hierarchical superstructures and are environmentally benign reaction media for the facile, “green” synthesis of shape-controlled inorganic nanocrystals. The reactive template-directed chemical transformation strategy provides a simple and versatile route to fabricate both hollow structures (e.g., spherical and nonspherical hollow particles) and 1D nanostructures (e.g., nanowires, nanotubes, and 2D networks assembled by nanorods). Colloidal crystals have been demonstrated to very effective templates for the facile solution-phase synthesis of novel inorganic structures with controlled micro- and nanopatterns, such as 3DOM single crystals, 2D patterned nanopillar arrays, and free-standing highly-ordered nanonets. In general, among various synthetic strategies, colloidal chemical synthesis in solution phase is advantageous in terms of cost, throughput, modulation of composition, and the potential for low-temperature and environmentally benign production.

Although a great success has been achieved in the colloidal chemical approaches towards inorganic micro- and nanostructures with controlled morphologies and patterns, there are still some big challenges ahead in this research area. Firstly, a more comprehensive understanding of the synthesis mechanisms and the development of general synthetic schemes for the desired micro- and nanostructures are of critical importance for the continuous success and advancement of this field. Secondly, further improvement in the colloidal chemical processes aimed at the large-scale synthesis of high-quality products with precisely controlled size, morphology, pattern as well as tunable composition, crystal structure, surface property is demanding. Thirdly, a more detailed investigation on the relationship between the property and the morphology and pattern of materials is needed for advancing the applications of the micro- and nanostructures obtained via colloidal chemical approaches. Finally, significant effort should be devoted to the colloidal chemical synthesis of useful materials with

designed shape and pattern targeting for applications in important technological fields including energy, environment, information, and biomedicine. It is clear that much more work needs to be done to realize the full potential of the colloidal chemical approaches towards advanced materials with desirable functions and applications, and excitement involved in the advancement of this powerful synthetic strategy will continue.

Acknowledgements

Financial support from NSFC (Grants 20873002, 20673007, 20633010, and 50821061), MOST (Grant 2007CB936201), and SRFDP (Grant 20070001018) is gratefully acknowledged.

References

[1] C. Burda, X. Chen, R. Narayanan, M.A. El-Sayed, Chem. Rev. 105 (2005) 1025.
[2] Y. Xia, Y. Xiong, B. Lim, S.E. Skrabalak, Angew. Chem. Int. Ed. 48 (2009) 60.
[3] A.R. Tao, S. Habas, P. Yang, Small 4 (2008) 310.
[4] Y.-w. Jun, J.-w. Seo, S.J. Oh, J. Cheon, Coord. Chem. Rev. 249 (2005) 1766.
[5] Y.-w. Jun, J.-s. Choi, J. Cheon, Angew. Chem. Int. Ed. 45 (2006) 3414.
[6] N. Tian, Z.-Y. Zhou, S.-G. Sun, Y. Ding, Z.L. Wang, Science 316 (2007) 732.
[7] I. Lee, F. Delbecq, R. Morales, M.A. Albiter, F. Zaera, Nat. Mater. 8 (2009) 132.
[8] B. Lim, M. Jiang, P.H.C. Camargo, E.C. Cho, J. Tao, X. Lu, Y. Zhu, Y. Xia, Science 324 (2009) 1302.
[9] H.G. Yang, C.H. Sun, S.Z. Qiao, J. Zou, G. Liu, S.C. Smith, H.M. Cheng, G.Q. Lu, Nature 453 (2008) 638.
[10] X. Han, Q. Kuang, M. Jin, Z. Xie, L. Zheng, J. Am. Chem. Soc. 131 (2009) 3152.
[11] J.J. Urban, D.V. Talapin, E.V. Shevchenko, C.R. Kagan, C.B. Murray, Nat. Mater. 6 (2007) 115.
[12] R.M. Erb, H.S. Son, B. Samanta, V.M. Rotello, B.B. Yellen, Nature 457 (2009) 999.
[13] H. Cölfen, M. Antonietti, Angew. Chem. Int. Ed. 44 (2005) 5576.
[14] S. Mann, Nat. Mater. 8 (2009) 781.
[15] P.D. Cozzoli, T. Pellegrino, L. Manna, Chem. Soc. Rev. 35 (2006) 1195.
[16] S.C. Glotzer, M.J. Solomon, Nat. Mater. 6 (2007) 557.
[17] Y. Xia, P. Yang, Y. Sun, Y. Wu, B. Mayers, B. Gates, Y. Yin, F. Kim, H. Yan, Adv. Mater. 15 (2003) 353.
[18] J. Goldberger, R. Fan, P. Yang, Acc. Chem. Res. 39 (2006) 239.
[19] C.M. Lieber, Z.L. Wang, MRS Bull. 32 (2007) 99.
[20] R. Yan, D. Gargas, P. Yang, Nat. Photonics 3 (2009) 569.
[21] X.W. Lou, L.A. Archer, Z.C. Yang, Adv. Mater. 20 (2008) 3987.
[22] W. Tong, C. Gao, J. Mater. Chem. 18 (2008) 3799.
[23] S.E. Skrabalak, J. Chen, Y. Sun, X. Lu, L. Au, C.M. Cobley, Y. Xia, Acc. Chem. Res. 41 (2008) 1587.
[24] Y. Ma, L. Qi, J. Colloid Interface Sci. 335 (2009) 1.
[25] C. Lopez, Adv. Mater. 15 (2003) 1679.
[26] A. Arsenault, S. Fournier-Bidoz, B. Hatton, H. Miguez, N. Tetreault, E. Vekris, S. Wong, S.M. Yang, V. Kitaev, G.A. Ozin, J. Mater. Chem. 14 (2004) 781.
[27] A. Stein, F. Li, N.R. Denny, Chem. Mater. 20 (2008) 649.
[28] L. Lu, A. Eychmüller, Acc. Chem. Res. 41 (2008) 244.
[29] J.L. Plawsky, J.K. Kim, E.F. Schubert, Mater. Today 12 (2009) 36.
[30] J. Henzie, J.E. Barton, C.L. Stender, T.W. Odom, Acc. Chem. Res. 39 (2006) 249.
[31] Y. Li, W. Cai, G. Duan, Chem. Mater. 20 (2008) 615.
[32] O. Sato, S. Kubo, Z.-Z. Gu, Acc. Chem. Res. 42 (2009) 1.
[33] Y. Yin, A.P. Alivisatos, Nature 437 (2005) 664.
[34] B.L. Cushing, V.L. Kolesnichenko, C.J. O'Connor, Chem. Rev. 104 (2004) 3893.
[35] M.-P. Pileni, Nat. Mater. 2 (2003) 145.
[36] L. Qi, in: P. Somasundaran (Ed.), Encyclopedia of Surface and Colloid Science, second ed., Taylor & Francis, New York, 2006, pp. 6183–6207.
[37] L. Qi, J. Ma, H. Cheng, Z. Zhao, J. Phys. Chem. B 101 (1997) 3460.
[38] H.-L. Sun, H. Shi, F. Zhao, L. Qi, S. Gao, Chem. Commun. (2005) 4339.
[39] H. Shi, L. Qi, J. Ma, H. Cheng, Chem. Commun. (2002) 1704.
[40] H. Shi, L. Qi, J. Ma, H. Cheng, J. Am. Chem. Soc. 125 (2003) 3450.
[41] H. Shi, X. Wang, N. Zhao, L. Qi, J. Ma, J. Phys. Chem. B 110 (2006) 748.
[42] H. Shi, L. Qi, J. Ma, H. Cheng, B. Zhu, Adv. Mater. 15 (2003) 1647.
[43] H. Shi, L. Qi, J. Ma, N. Wu, Adv. Funct. Mater. 15 (2005) 442.
[44] B. Abécassis, F. Testarda, T. Zemb, Soft Matter 5 (2009) 974.
[45] Y. Xing, M. Li, S.A. Davis, A.J. Patil, S. Mann, Soft Matter 2 (2006) 603.
[46] B. Abécassis, F. Testard, L. Arleth, S. Hansen, I. Grillo, T. Zemb, Langmuir 23 (2007) 9983.
[47] R. Biswas, A.R. Das, T. Pradhan, D. Touraud, W. Kunz, S. Mahiuddin, J. Phys. Chem. B 112 (2008) 6620.
[48] S.-M. Lee, Y.-W. Jun, S.-N. Cho, J. Cheon, J. Am. Chem. Soc. 124 (2002) 11244.
[49] N. Zhao, L. Qi, Adv. Mater. 18 (2006) 359.
[50] N. Zhao, Y. Wei, N. Sun, Q. Chen, J. Bai, L. Zhou, Y. Qin, M. Li, L. Qi, Langmuir 24 (2008) 991.
[51] L. Fan, R. Guo, Cryst. Growth Des. 8 (2008) 2150.
[52] A.A. Firooza, A.R. Mahjouba, A.A. Khodadadib, Sens. Actuators B: Chem. 141 (2009) 89.
[53] U. Jeong, P.H.C. Camargo, Y.H. Lee, Y. Xia, J. Mater. Chem. 16 (2006) 3893.
[54] H. Niu, M. Gao, Angew. Chem. Int. Ed. 45 (2006) 6462.
[55] H. Tong, Y. Zhu, L. Yang, L. Li, L. Zhang, Angew. Chem. Int. Ed. 45 (2006) 7739.
[56] H. Wang, L. Qi, Adv. Funct. Mater. 18 (2008) 1249.
[57] T. Huang, L. Qi, Nanotechnology 20 (2009) 025606.
[58] Y. Ma, L. Qi, J. Ma, H. Cheng, Adv. Mater. 16 (2004) 1023.
[59] J. Ye, H. Zhang, R. Yang, X. Li, L. Qi, Small 6 (2010) 296.
[60] L. Li, N. Sun, Y. Huang, Y. Qin, N. Zhao, J. Gao, M. Li, H. Zhou, L. Qi, Adv. Funct. Mater. 18 (2008) 1194.
[61] Y. Yin, R.M. Rioux, C.K. Erdonmez, S. Hughes, G.A. Somorjai, A.P. Alivisatos, Science 304 (2004) 711;
H. Fan, U. Gosele, M. Zacharias, Small 3 (2007) 1660.
[62] J. Gao, Q. Li, H. Zhao, L. Li, C. Liu, Q. Gong, L. Qi, Chem. Mater. 20 (2008) 6263.
[63] L. Li, R. Cao, Z. Wang, J. Li, L. Qi, J. Phys. Chem. C 113 (2009) 18075.
[64] J. Yang, L. Qi, C. Lu, J. Ma, H. Cheng, Angew. Chem. Int. Ed. 44 (2005) 598.
[65] C. Lu, L. Qi, J. Yang, X. Wang, D. Zhang, J. Xie, J. Ma, Adv. Mater. 17 (2005) 2562.
[66] H. Cao, X. Qian, C. Wang, X. Ma, J. Yin, Z. Zhu, J. Am. Chem. Soc. 127 (2005) 16024.
[67] S. Jiao, L. Xu, K. Jiang, D. Xu, Adv. Mater. 18 (2006) 1174.
[68] L. Ye, C. Wu, W. Guo, Y. Xie, Chem. Commun. (2006) 4738.
[69] J. Fei, Y. Cui, X. Yan, W. Qi, Y. Yang, K. Wang, Q. He, J. Li, Adv. Mater. 20 (2008) 452.
[70] S. Liu, X. Wu, B. Hu, J. Gong, S.-H. Yu, Cryst. Growth Des. 9 (2009) 1511.
[71] S.-M. Yang, S.G. Jang, D. Choi, S. Kim, H.K. Yu, Small 2 (2006) 458.
[72] G. Zhang, D. Wang, Chem. Asian J. 4 (2009) 236.
[73] J. Aizenberg, Adv. Mater. 16 (2004) 1295.
[74] Z. Li, J. Wang, B. Gu, Phys. Rev. B 58 (1998) 3721.
[75] Z. Xie, L. Sun, G. Han, Z. Gu, Adv. Mater. 20 (2008) 3601.
[76] J. Aizenberg, D.A. Muller, J.L. Grazul, D.R. Hamann, Science 299 (2003) 1205.
[77] C. Li, L. Qi, Angew. Chem. Int. Ed. 47 (2008) 2388.
[78] A.S. Finnemore, M.R.J. Scherer, R. Langford, S. Mahajan, S. Ludwigs, F.C. Meldrum, U. Steiner, Adv. Mater. 21 (2009) 3928.
[79] H. Cölfen, Angew. Chem. Int. Ed. 47 (2008) 2351.
[80] H.J. Fan, P. Werner, M. Zacharias, Small 2 (2006) 700.
[81] C. Li, G. Hong, P. Wang, D. Yu, L. Qi, Chem. Mater. 21 (2009) 891.
[82] C. Li, G. Hong, L. Qi, Chem. Mater. 22 (2010) 476.